

Exhibit 2



US 2005/0072234A1

(19) **United States**(12) **Patent Application Publication** (10) Pub. No.: **US 2005/0072234 A1**
Zhu et al. (43) Pub. Date: **Apr. 7, 2005**(54) **SYSTEM AND METHOD FOR DETECTING
STRUCTURAL DAMAGE**(76) Inventors: Weidong Zhu, Elkridge, MD (US);
Guangyao Xu, Baltimore, MD (US);
Nengan Zheng, Baltimore, MD (US);
Benjamin Haynes Emory, Baltimore,
MD (US); Chun Nam Wong, Lubbock,
TX (US)Correspondence Address:
FLESHNER & KIM, LLP
P.O. Box 221200
Chantilly, VA 20153-1200 (US)

(21) Appl. No.: 10/849,571

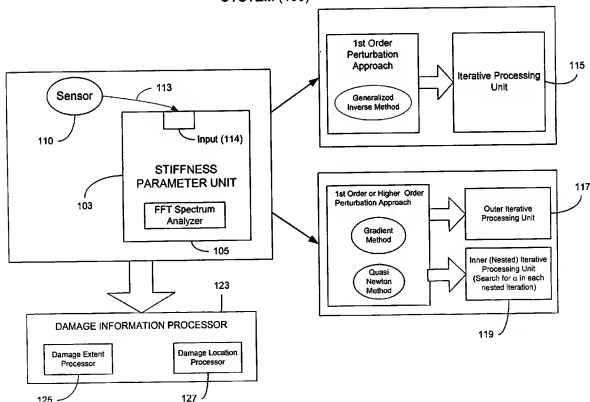
(22) Filed: May 20, 2004

Related U.S. Application Data(60) Provisional application No. 60/471,873, filed on May
20, 2003. Provisional application No. 60/512,656,
filed on Oct. 20, 2003.**Publication Classification**(51) Int. Cl.⁷ G01H 1/14; G01M 7/08

(52) U.S. Cl. 73/579; 73/12.01; 702/56

(57) **ABSTRACT**

A system and method for detecting structural damage is provided that utilizes a general order perturbation methodology involving multiple perturbation parameters. The perturbation methodology is used iteratively in conjunction with an optimization method to identify the stiffness parameters of structures using natural frequencies and/or mode shape information. The stiffness parameters are then used to determine the location and extent of damage in a structure. A novel stochastic model is developed to model the random impact series produced manually or to generate a random impact series in a random impact device. The random impact series method or the random impact device can be used to excite a structure and generate vibration information used to obtain the stiffness parameters of the structure. The method or the device can also be used for modal testing purposes. The random impact device is a high energy, random, and high signal-to-noise ratio system.

SYSTEM (100)

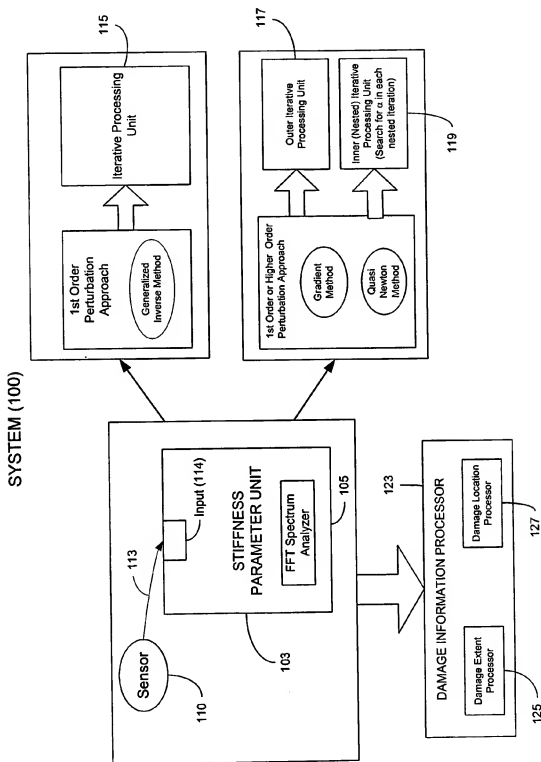


Figure 1A

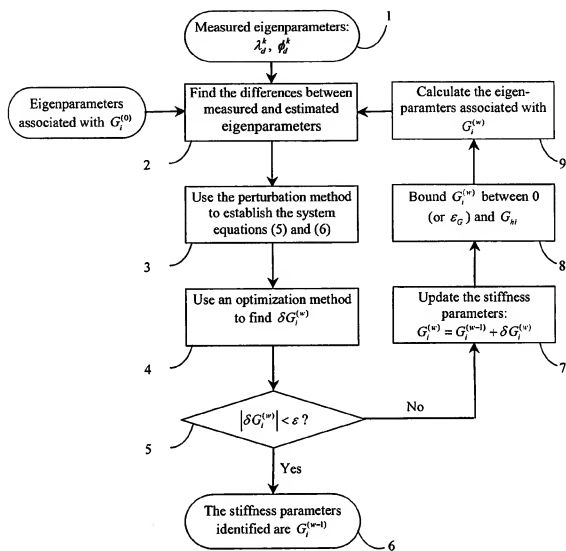


Figure 1B

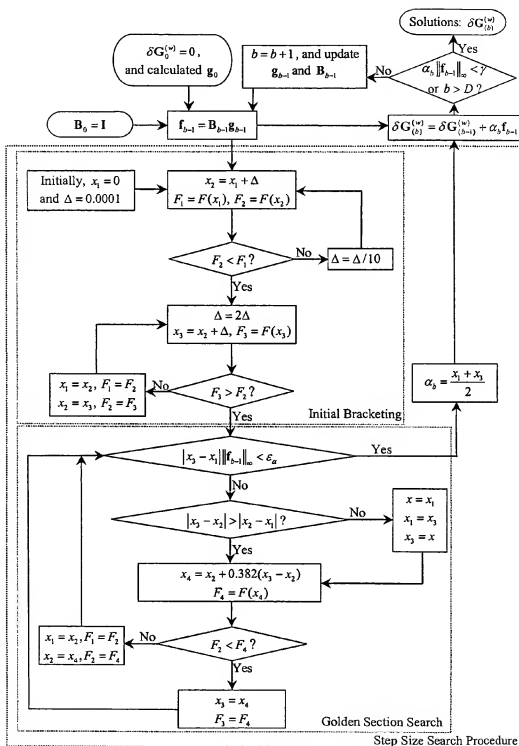


Figure 2

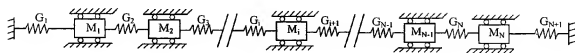


Figure 3

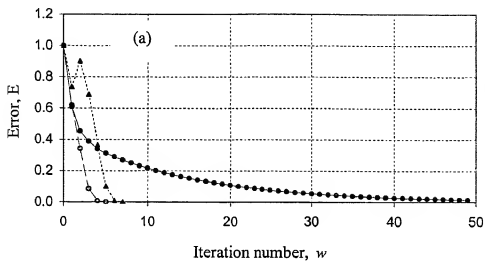


Fig. 4A

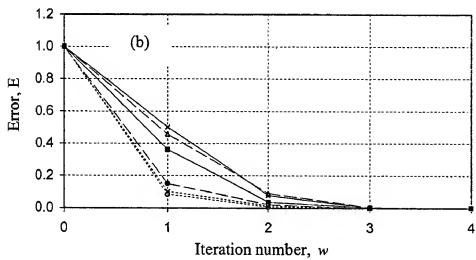


Fig. 4B

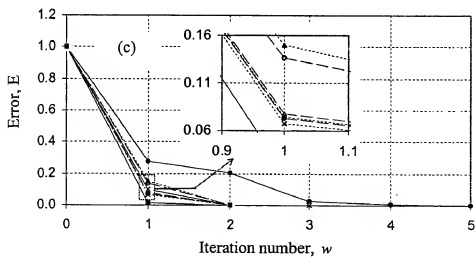


Fig. 4C

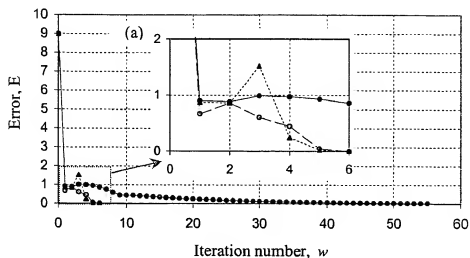


Fig. 5A

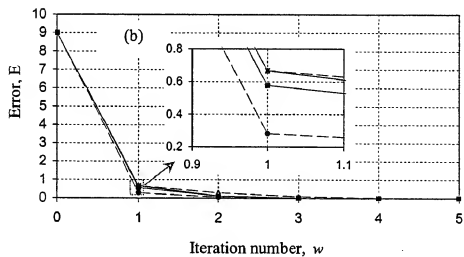


Fig. 5B

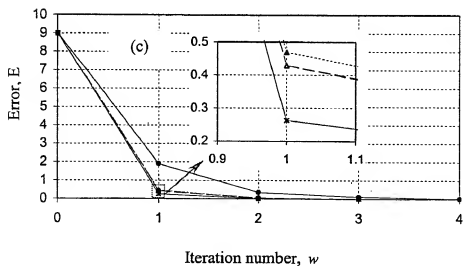


Fig. 5C

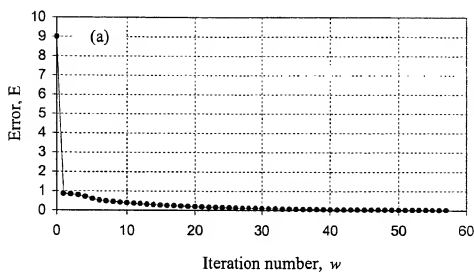


Fig. 6A

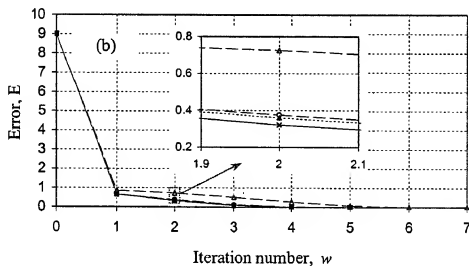


Fig. 6B

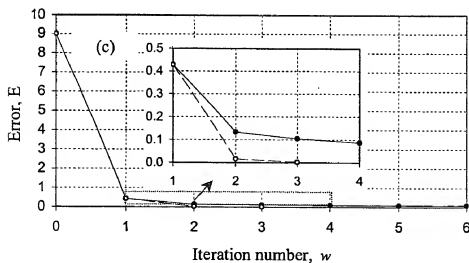


Fig. 6C

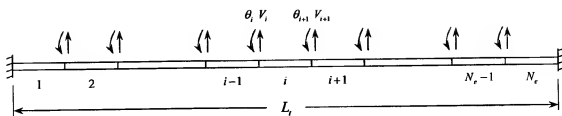


Figure 7

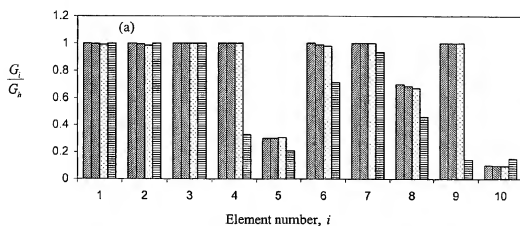


Fig. 8A

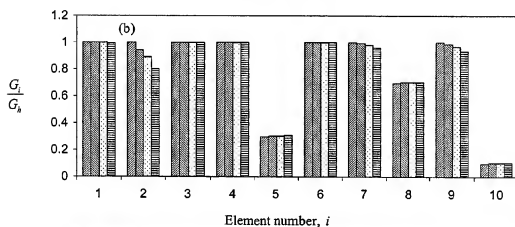


Fig. 8B

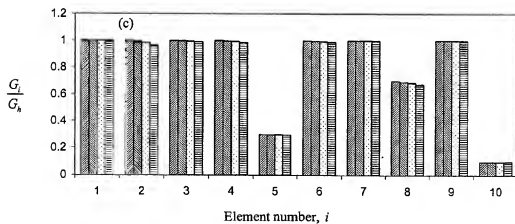
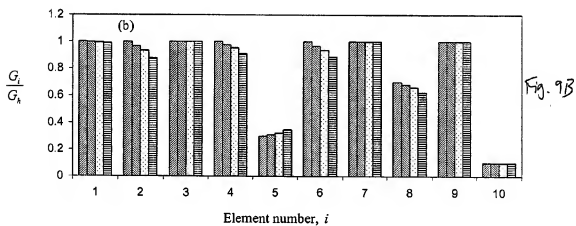
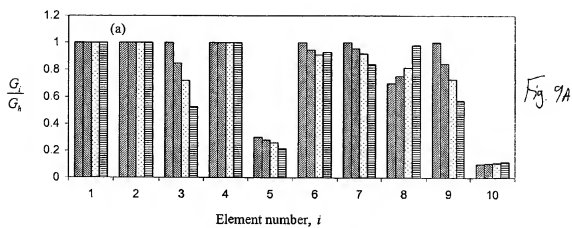


Fig. 8C



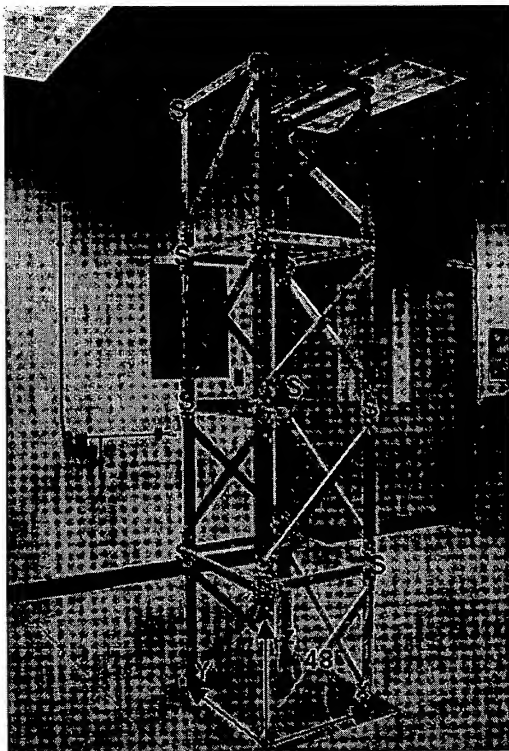


Figure 10

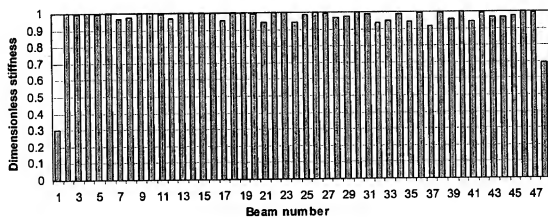


Figure 11

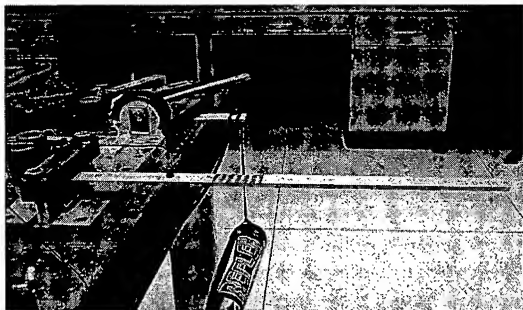


Figure 12

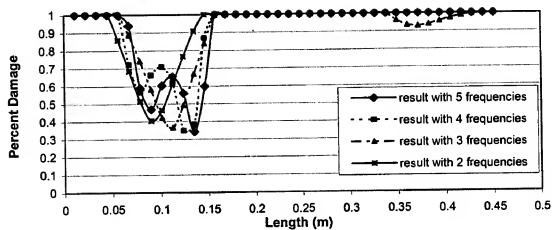


Figure 13

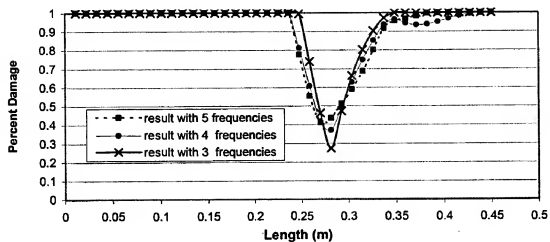


Figure 14

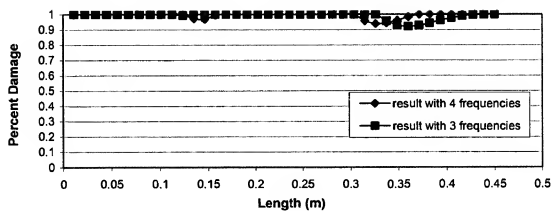


Figure 15

Damage at 22.5 cm from base



Figure 16

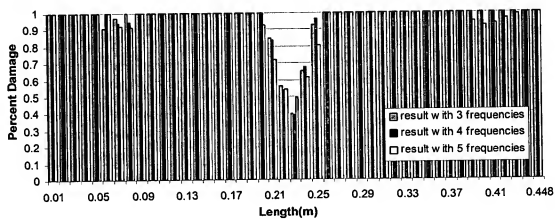


Figure 17

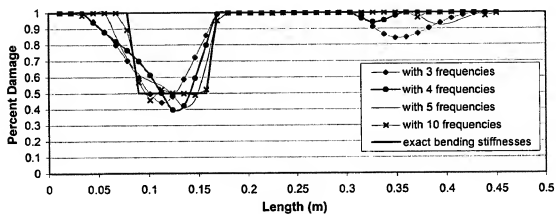


Figure 18

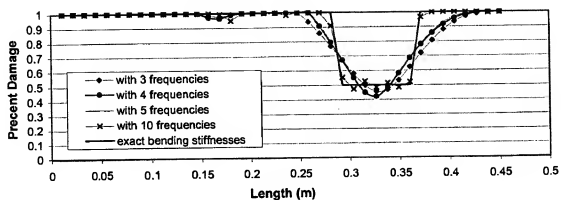


Figure 19

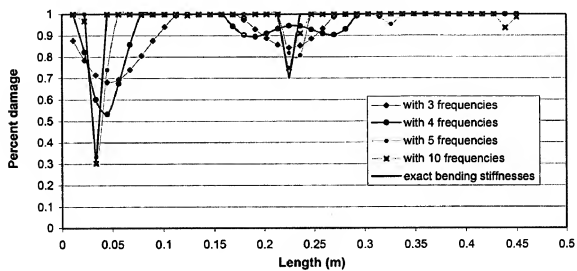


Figure 20

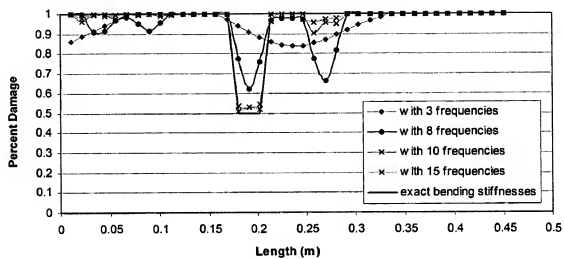


Figure 21

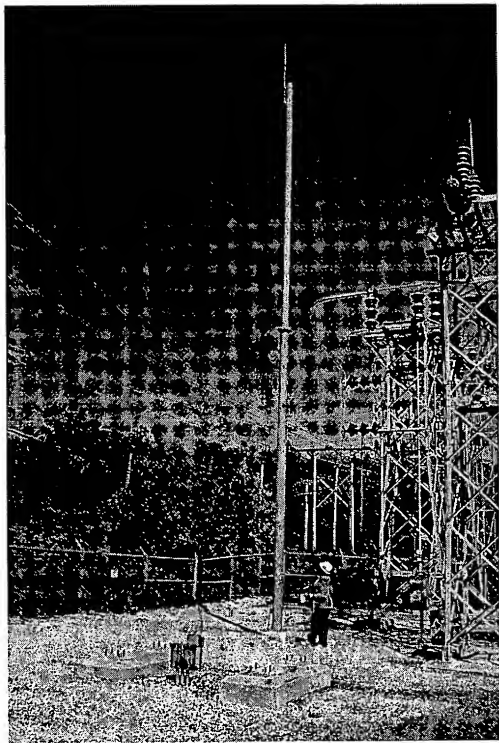


Figure 22

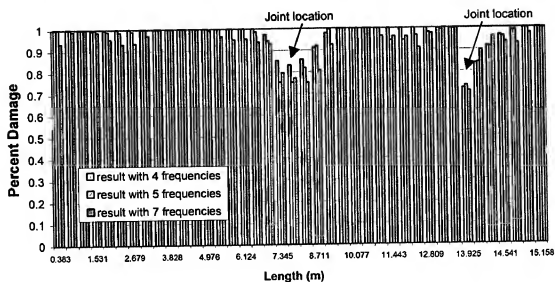


Figure 23

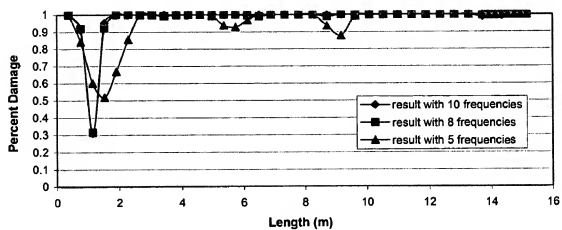


Figure 24

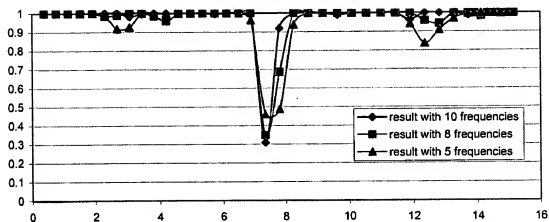


Figure 25

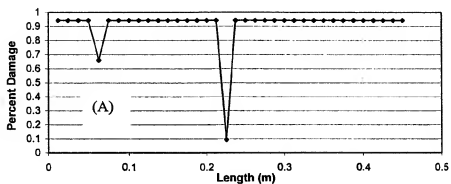


Fig. 26A

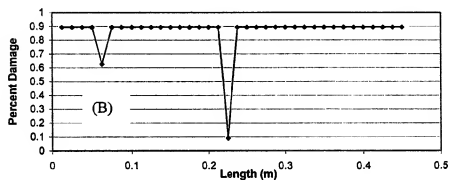


Fig. 26B

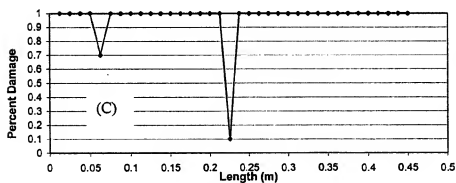


Fig. 26C

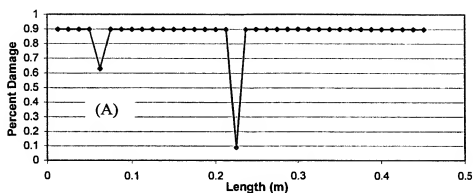


Fig. 27A

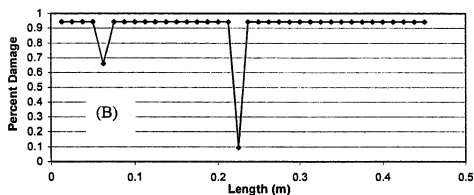


Fig. 27B

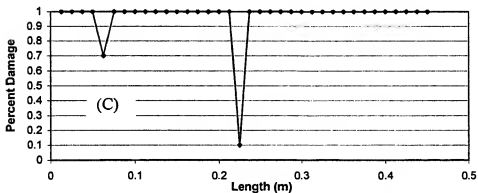


Fig. 27C

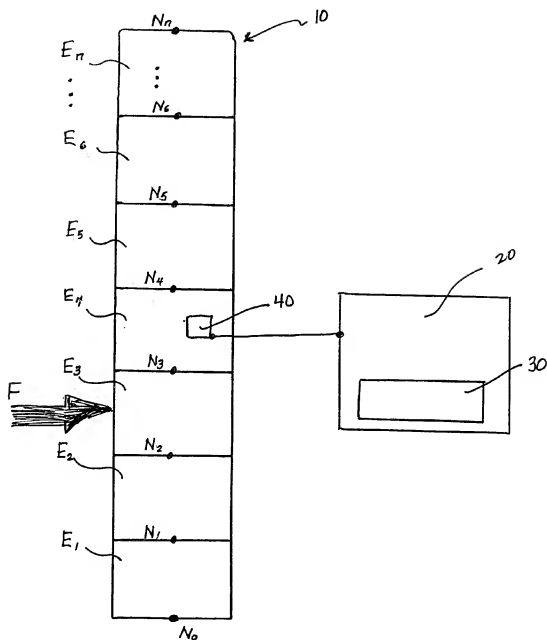


Figure 28

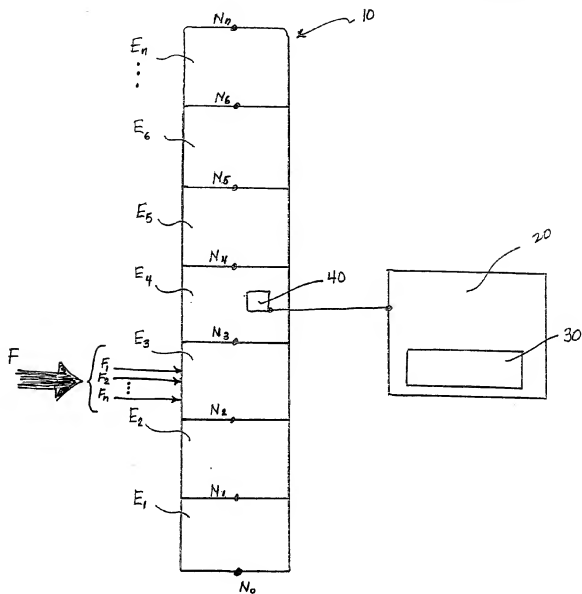


Figure 29

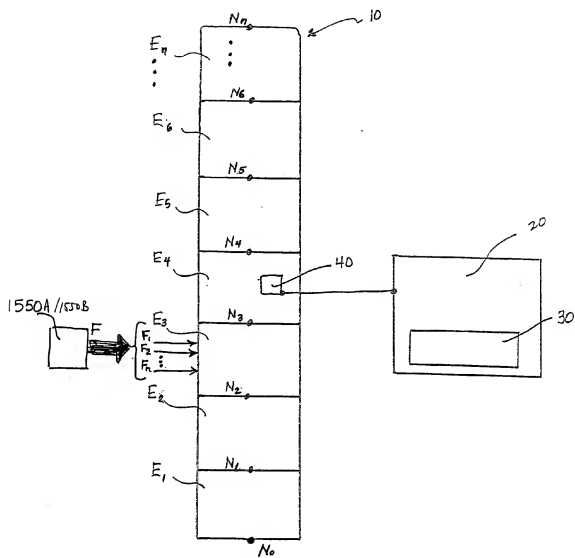


Figure 30

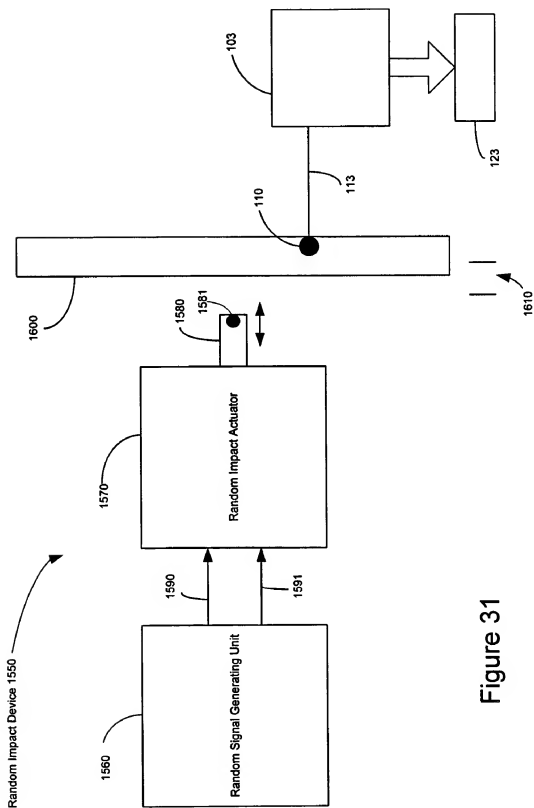


Figure 31

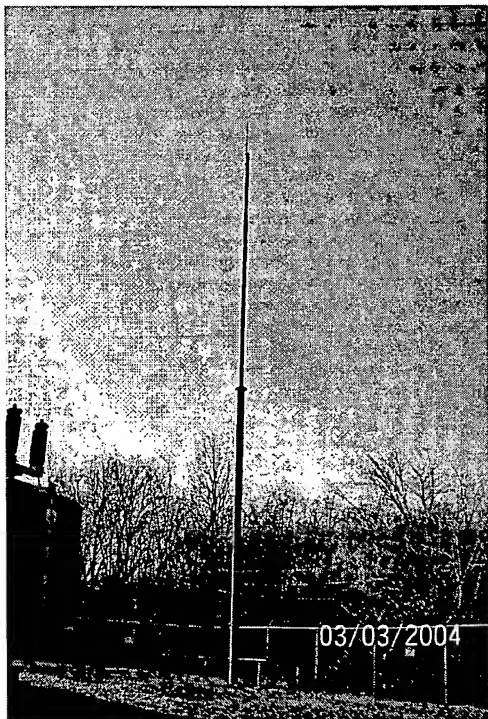


Figure 32

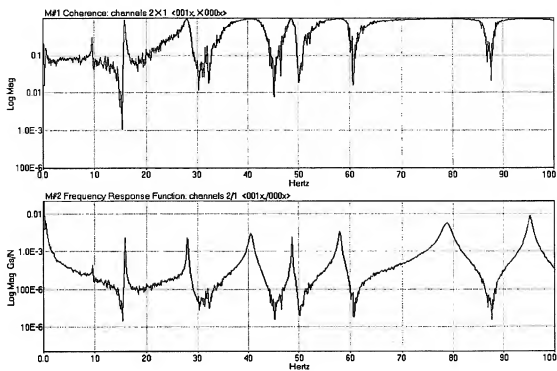


Figure 33A

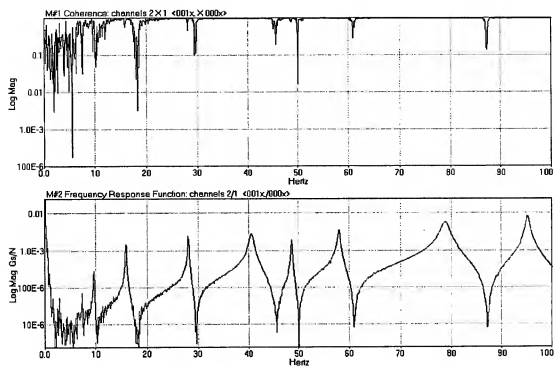


Figure 33B

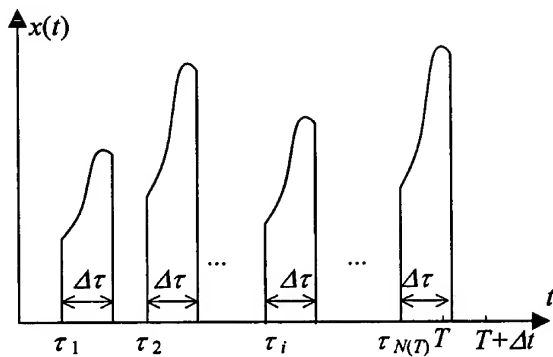


Figure 34

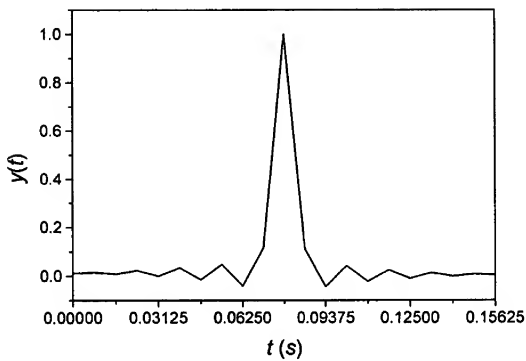


Figure 35

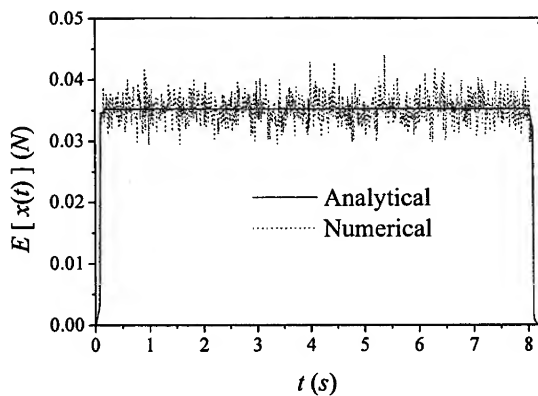


Figure 36

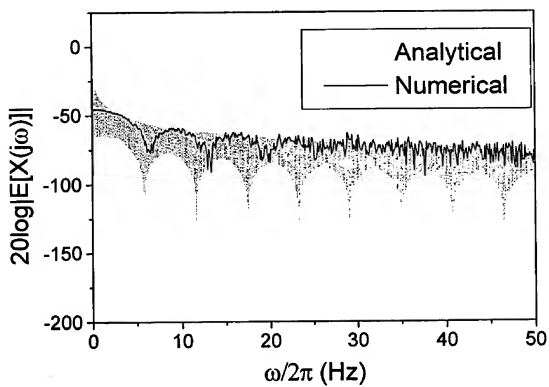


Figure 37

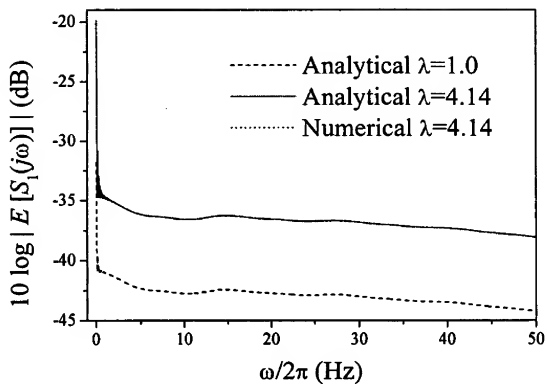


Figure 38

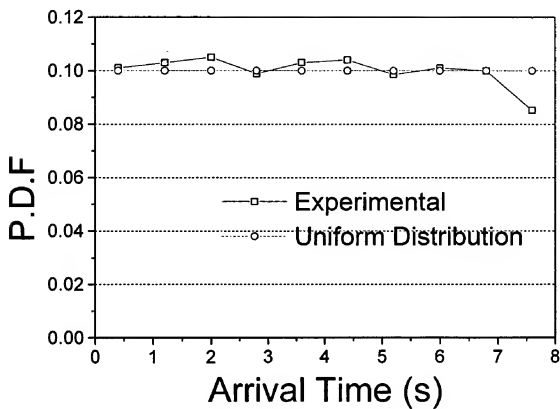


Figure 39

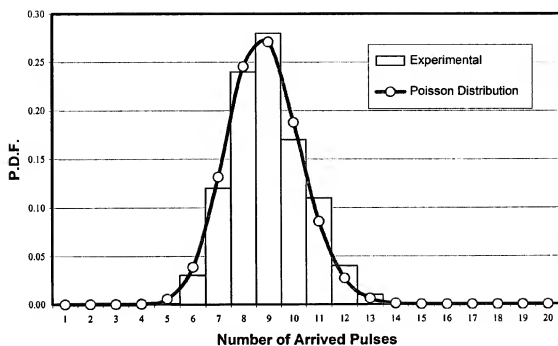


Figure 40

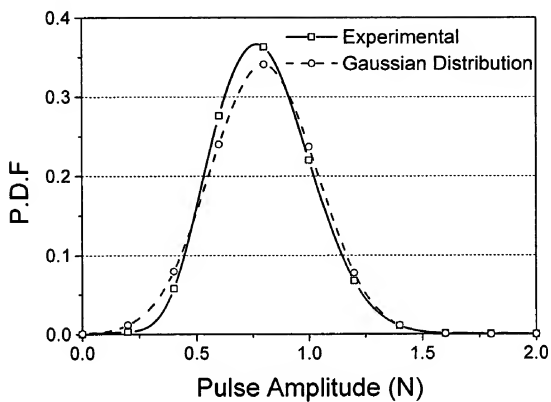


Figure 41

SYSTEM AND METHOD FOR DETECTING STRUCTURAL DAMAGE

[0001] This application claims priority to U.S. Provisional Patent Application Ser. No. 60/471,873 filed May 20, 2003 and U.S. Provisional Patent Application Ser. No. 60/512,656 filed Oct. 10, 2003, which are both incorporated herein by reference.

BACKGROUND OF THE INVENTION

[0002] 1. Field of the Invention

[0003] The invention relates to a method and apparatus for detecting structural damage, and, more specifically, to a method and apparatus for detecting structural damage using changes in natural frequencies and/or mode shapes.

[0004] 2. Background of the Related Art

[0005] Damage in a structure can be defined as a reduction in the structure's load bearing capability, which may result from a deterioration of the structure's components and connections. All load bearing structures continuously accumulate structural damage, and early detection, assessment and monitoring of this structural damage and appropriate removal from service is the key to avoiding catastrophic failures, which may otherwise result in extensive property damage and cost.

[0006] A number of conventional non-destructive test (NDT) methods are used to inspect load bearing structures. Visual inspection of structural members is often unquantifiable and unreliable, especially in instances where access to damaged areas may be impeded or damage may be concealed by paint, rust, or other coverings. Penetrant testing (PT) requires that an entire surface of the structure be covered with a dye solution, and then inspected. PT reveals only surface cracks and imperfections, and can require a large amount of potentially hazardous dye be applied and disposed of. Similarly, magnetic particle testing (MT) requires that an entire surface of the structure be treated, can be applied only to ferrous materials, and detects only relatively shallow cracks. Further, due to the current required to generate a strong enough magnetic field to detect cracks, MT is not practically applied to large structures. Likewise, eddy current testing (ET) uses changes in the flow of eddy currents to detect flaws, and only works on materials that are electrically conductive. Ultrasonic testing (UT) uses transmission of high frequency sound waves into a material to detect imperfections. Results generated by all of these methods can be skewed due to surface conditions, and cannot easily isolate damage at joints and boundaries of the structure. Unless a general vicinity of a damage location is known prior to inspection, none of these methods are easily or practically applied to large structures which are already in place and operating. On the other hand, resonant inspection methods are not capable of determining the extent or location of damage, and is used only on a component rather than a assembled structure. None of the above NDT methods are easily or practically applied to large structures requiring a high degree of structural integrity.

[0007] Because of these shortfalls in existing NDT methods when inspecting relatively large structures, structural damage detection using changes in vibration characteristics has received much attention in recent years. Vibration based health monitoring for rotating machinery is a relatively

mature technology, using a non-model based approach to provide a qualitative comparison of current data to historical data. However, this type of vibration based damage testing does not work for most structures. Rather, vibration based damage detection for structures is model based, comparing test data to analytical data from finite element models to detect the location(s) and extent of damage. Vibration based damage detection methods fall into three basic categories. The first of these is direct methods such as optimal matrix updating algorithms, which identify damage location and extent in a single iteration. Because of the single iteration, these methods are not accurate in detecting a large level of damage. The second category is iterative methods. The methodology has only been for updating modeling, which determines modified structural parameters iteratively by minimizing differences between model and test data. The third category includes control-based eigenstructure assignment methods, which have the similar limitation to that of the direct methods indicated above and are not accurate in detecting a large level of damage. None of these current vibration based methods have been incorporated into an iterative algorithm that can detect small to large levels of damage, and the vibration based approach for structures remains an immature technology area which is not readily available on a commercial basis.

SUMMARY OF THE INVENTION

[0008] An object of the invention is to solve at least the above problems and/or disadvantages and to provide at least the advantages described hereinafter.

[0009] Another object of the invention is to provide a system and method for detecting structural damage based on changes in natural frequencies and/or mode shapes.

[0010] An advantage of the system and method as embodied and broadly described herein is that it can be applied to a large operating structure with a large number (thousands or more) of degrees of freedom.

[0011] Another advantage of the system and method as embodied and broadly described herein is that it can accurately detect the location(s) and extent of small to large levels of damage and is especially useful for detecting a large level of damage with severe mismatch between the eigenparameters of the damaged and undamaged structures.

[0012] Another advantage of the system and method as embodied and broadly described herein is that it can work with a limited number of measured vibration modes.

[0013] Another advantage of the system and method as embodied and broadly described herein is that it can use measurement at only a small number of locations compared to the degrees of freedom of the system. A modified eigenvector expansion method is used to deal with the incomplete eigenvector measurement problem arising from experimental measurement of a lesser number of degrees of freedom than that of the appropriate analytical model.

[0014] Another advantage of the system and method as embodied and broadly described herein is that it can be applied to structures with slight nonlinearities such as opening and closing cracks. The random shaker test or the random impact series method can be used to average out slight nonlinearities and extract linearized natural frequencies and/or mode shapes of a structure.

[0015] Another advantage of the system and method as embodied and broadly described herein is that it can handle structures with closely spaced vibration modes, where mode switching can occur in the damage detection process.

[0016] Another advantage of the system and method as embodied and broadly described herein is that it can handle different levels of measurement noise with estimation errors within the noise levels.

[0017] Another advantage of the system and method as embodied and broadly described herein is that the damage detection method and the vibration testing methods such as the random impact series method enables damage detection and assessment to be automated, thus improving the reliability/integrity of results.

[0018] Another advantage of the system and method as embodied and broadly described herein is that damage detection and assessment may be automated in the field so that structural health can be monitored at central location and useful service life may be optimized.

[0019] Another advantage of the system and method as embodied and broadly described herein is that the random impact series method enables the modal parameters such as natural frequencies and/or mode shapes to be measured for a large structure or a structure in the field when there are noise effects such as those arising from the wind or other ambient excitation.

[0020] Additional advantages, objects, and features of the invention will be set forth in part in the description which follows and in part will become apparent to those having ordinary skill in the art upon examination of the following or may be learned from practice of the invention. The objects and advantages of the invention may be realized and attained as particularly pointed out in the appended claims.

BRIEF DESCRIPTION OF THE DRAWINGS

[0021] The invention will be described in detail with reference to the following drawings in which like reference numerals refer to like elements herein:

[0022] FIG. 1A shows a system 100 for detection of structural damage according to one embodiment of the invention;

[0023] FIG. 1B is a flowchart of an inverse algorithm for identifying stiffness parameters of a damaged structure from a select set of measured eigenparameters, in accordance with an embodiment of the invention;

[0024] FIG. 2 is a flowchart of a quasi-Newton method for finding an optimal solution to the system equations shown in the flowchart of FIG. 1B, in accordance with an embodiment of the invention;

[0025] FIG. 3 is a schematic view of a serial mass-spring system;

[0026] FIGS. 4A-4C illustrate estimation errors in a series of iterations for a low order system with a small level of damage;

[0027] FIGS. 5A-5C illustrate estimation errors in a series of iterations for a low order system with a large level of damage;

[0028] FIGS. 6A-6C illustrate estimation errors in a series of iterations for a large order system with a large level of damage;

[0029] FIG. 7 illustrates a finite element model of a fixed-fixed beam;

[0030] FIGS. 8A-8C illustrate the estimated stiffness parameters with complete eigenvector measurements and different noise levels for a ten element beam with a large level of damage;

[0031] FIGS. 9A-9B illustrate stiffness parameters with reduced eigenvector measurements and different noise levels for a ten element beam with a large level of damage;

[0032] FIG. 10 illustrates a modular, four bay space frame;

[0033] FIG. 11 illustrates the estimated dimensionless stiffnesses for the damaged frame as shown in FIG. 11;

[0034] FIG. 12 illustrates a cantilever aluminum beam test specimen with uniform damage in approximately 5 elements;

[0035] FIG. 13 illustrates the experimental results for the estimated bending stiffnesses of all the elements of a cantilever aluminum beam test specimen with the actual damage between 10 cm and 15 cm from the cantilevered end using a 40-element finite element model;

[0036] FIG. 14 illustrates the experimental results for the estimated bending stiffnesses of all the elements of a cantilevered aluminum beam test specimen with the actual damage between 25 cm and 30 cm from the cantilevered end using a 40-element finite element model;

[0037] FIG. 15 illustrates the experimental results for the estimated bending stiffnesses of all the elements of an undamaged cantilever aluminum beam test specimen using a 40-element finite element model;

[0038] FIG. 16 illustrates a cantilever aluminum beam test specimen with a narrow cut;

[0039] FIG. 17 illustrates the experimental results for the estimated bending stiffnesses of all the elements of the test specimen as shown in FIG. 16 using a 45-element finite element model;

[0040] FIG. 18 illustrates the estimated bending stiffnesses of all the elements of the cantilever aluminum with simulated damage between 9 cm and 15.75 cm from the cantilevered end using a 40-element finite element model;

[0041] FIG. 19 illustrates the estimated bending stiffnesses of all the elements of the cantilever aluminum beam with simulated damage between 29.25 cm and 36 cm from the cantilevered end using a 40-element finite element model;

[0042] FIG. 20 illustrates the estimated bending stiffnesses of all the elements of the cantilever aluminum beam with multiple simulated damage—one at the 3rd element and the other at the 20th element;

[0043] FIG. 21 illustrates the estimated bending stiffnesses of all the elements of the cantilever aluminum beam with simulated uniform damage from the 16th to the 18th element;

[0044] FIG. 22 illustrates a 50-foot lightning mast test specimen with an eccentric spike at the top;

[0045] FIG. 23 illustrates the experimental results for the estimated bending stiffnesses of all the elements of the lightning mast as shown in FIG. 22;

[0046] FIG. 24 illustrates the estimated bending stiffnesses of all the elements of the lightning mast as shown in FIG. 22 with simulated damage between 0.76 m and 1.125 m from the ground using a 40-element finite element model;

[0047] FIG. 25 illustrates the estimated bending stiffnesses of all the elements of the lightning mast as shown in FIG. 42 with simulated damage between 6.89 m and 7.35 m from the ground using a 40-element finite element model;

[0048] FIGS. 26A-26C illustrate the estimated bending stiffnesses of all the elements of a cantilever aluminum beam using the first regularization method;

[0049] FIGS. 27A-27C illustrate the estimated bending stiffnesses of all the elements of a cantilever aluminum beam using the second regularization method;

[0050] FIG. 28 illustrates an example of a practical application of the damage detection method of FIG. 1A, in accordance with an embodiment of the invention;

[0051] FIG. 29 illustrates the application of a series of random impacts to the practical application of the damage detection method of FIG. 1A, in accordance with an embodiment of the invention;

[0052] FIG. 30 illustrates a system for applying the series of random impacts shown in FIG. 29 to the practical application of the damage detection method of FIG. 1A, in accordance with an embodiment of the invention;

[0053] FIG. 31 is a block diagram of one preferred embodiment of the random impact device of FIG. 30;

[0054] FIG. 32 illustrates a lightning mast specimen;

[0055] FIGS. 33A-33B are graphical representations of coherence and FRF from single and multiple impact tests of the mast shown in FIG. 32;

[0056] FIG. 34 illustrates a random series of pulses with the same deterministic shape and random amplitudes and arrival times;

[0057] FIG. 35 illustrates an average normalized shape function of force pulses;

[0058] FIGS. 36-38 are graphical representations of analytical and numerical solutions;

[0059] FIG. 39 shows the comparison of the probability density function (PDF) of the experimental arrival time with that from uniform distribution;

[0060] FIG. 40 shows the comparison of the experimental and analytical PDFs for the number of arrived pulses; and

[0061] FIG. 41 shows the comparison of the experimental and analytical PDFs for the pulse amplitudes.

DETAILED DESCRIPTION OF PREFERRED EMBODIMENTS

[0062] Commonly measured modal parameters, such as natural frequencies and mode shapes, are functions of physical

properties of a particular structure. Therefore, changes in these physical properties, such as reductions in stiffness resulting from the onset of cracks or a loosening of a connection, will cause detectable changes in these modal parameters. Thus, if the changes in these parameters are indicators of damage, vibration based damage detection may be, simplistically, reduced to a system identification problem. However, a number of factors have made vibration based damage detection difficult to implement in practice in the past.

[0063] The system and method for detecting structural damage as embodied and broadly described herein is motivated by the observed advantages of vibration based damage detection over currently available technologies. It is well understood that this system and method may be effectively applied to damage detection and assessment for substantially all types and configurations of structures, including, but not limited to, simple beams, hollow tubes, trusses, frames, and the like. However, simply for ease of discussion, the system and method will first be discussed with respect to three examples—a mass-spring model, a beam, and a space frame—for conceptualization purposes. The system and method will later be applied lightning masts in electric substations.

[0064] FIG. 1A shows a system 100 for detecting structural damage according to one embodiment of the invention. System 100 includes a stiffness parameter unit 103 for detecting stiffness of a structure in question. Stiffness parameter unit 103 may include a spectrum analyzer or any other device capable of receiving vibration information and providing natural frequency and/or mode shape data. One example might be a spectrum analyzer capable of performing a fast fourier transform (FFT) and with modal analysis software for deriving mode shape data from vibration information received from sensor 110 if mode shape information is needed. A roving sensor technique or multiple sensors may need to be used if mode shape information needs to be used. If mode shape information is desired, a sensor should be provided at the tip of the hammer or device used to excite the structure. This sensor should be configured to send data to the spectrum analyzer in order to obtain the frequency response function, which the spectrum analyzer (modal analysis software) uses to obtain mode shape information. Stiffness parameter unit 103 is configured to receive vibration information output from the sensor 110 via sensor coupler 113 and input 114. Sensor coupler 113 could be a wire, optical fiber or even a wireless connection between sensor 110 and stiffness parameter unit 103.

[0065] Stiffness parameter unit 103 may include an iterative processing unit 115 capable of determining stiffness parameters using a first order perturbation approach and the generalized inverse method. The first order perturbation approach can include using natural frequencies and/or mode shapes of the structure according to a preferred embodiment of the invention. Iterative processing unit 115 may be capable of converging to a correct result for the output of stiffness parameters even when the system is undetermined. Stiffness parameter unit 103 may further include an outer iterative processing unit 117 and an inner (nested) iterative processing unit 119 which may operate using a first or higher order perturbation approach and a gradient or quasi-Newton method to be discussed below. Stiffness parameter unit 103 outputs stiffness parameters to damage

information processor 123. Damage information processor includes a damage extent processor 125 and a damage location processor 127. Damage location processor 127 outputs the location(s) of damage and damage extent processor 125 outputs the extent of damage.

[0066] System 100 using the iterative processing units 115 or 117 and 119 is capable of determining the stiffness parameters and ultimately the location(s) and extent of damage for structures with a largest dimension less than 50 meters, 25 meters, 10 meters, 2.5 meters and even 1.5 meters. Examples of this are provided herein.

[0067] The system and method may include a multiple-parameter, general order perturbation method, in which the changes in the stiffness parameters are used as the perturbation parameters. By equating the coefficients of like-order terms involving the same perturbation parameters in the normalization relations of eigenvectors and the eigenvalue problem, the perturbation problem solutions of all orders may be derived, and the sensitivities of all eigenparameters may be obtained. The perturbation method may be used in an iterative manner with an optimization method to identify the stiffness parameters of structures.

[0068] Methodology

[0069] This method presented below can simultaneously identify all the unknown stiffness parameters and is formulated as a damage detection problem. Since the effects of the changes in the inertial properties of a damaged structure are usually relatively small, only the changes in the stiffness properties due to structural damage are considered.

[0070] Consider a N degree-of-freedom, linear, time-invariant, self-adjoint system with distinct eigenvalues. The stiffness parameters of the undamaged structure are denoted by G_{i1} ($i=1, 2, \dots, m$), where m is the number of the stiffness parameters. Structural damage is characterized by reductions in the stiffness parameters. The estimated stiffness parameters of the damaged structure before each iteration are denoted by G_i ($i=1, 2, \dots, m$), and its stiffness matrix, which depends linearly on G_i , is denoted by $K=K(G)$, where $G=[G_1, G_2, \dots, G_m]^T$. Here the superscript T denotes matrix transpose. The eigenvalue problem of the structure with stiffness parameters G_i is

$$K\phi^k = \lambda^k M \phi^k \quad (1)$$

[0071] where M is the constant mass matrix, and $\lambda^k = \lambda^k(G)$ and $\phi^k = \phi^k(G)$ ($k=1, 2, \dots, N$) are the k -th eigenvalue and mass-normalized eigenvector respectively. It is noted that $\lambda_k = \omega_k^2$, where ω_k is the k -th natural frequency of the structure. The normalized eigenvectors of (1) satisfy the orthonormality relations

$$(\phi^j)^T M \phi^k = \delta_{kj} \quad (\phi^j)^T K \phi^k = \lambda^k \delta_{kj} \quad (2)$$

[0072] where $1 \leq j \leq N$ and δ_{kj} is the Kronecker delta. Before the first iteration, the initial stiffness parameters of the damaged structure are assumed to be $G_i^{(0)} = \alpha_i^0 G_{i1}$ ($i=1, 2, \dots, m$), where $0 < \alpha_i^0 \leq 1$, and the eigenvalue problem in (1) corresponds to that of the structure with stiffness parameters $G_i^{(0)}$. If there is no prior knowledge of the integrity of the structure, one can start the iteration from the stiffness parameters of the undamaged structure and set $\alpha_i^0 = 1$. Let G_{i1} ($i=1, 2, \dots, m$) denote the stiffness parameters of the

damaged structure. The eigenvalue problem of the damaged structure is

$$K_i \phi_i^k = \lambda_i^k M \phi_i^k \quad (3)$$

[0073] where $K_i = K(G_i)$ is the stiffness matrix with $G_i = [G_{i1}, G_{i2}, \dots, G_{im}]^T$, and $\lambda_i^k = \lambda^k(G_i)$ and $\phi_i^k = \phi^k(G_i)$ are the k -th eigenvalue and mass-normalized eigenvector respectively. The stiffness matrix K_i is related to K through the Taylor expansion

$$K_i = K(G_i) = K + \sum_{j=1}^m \frac{\partial K}{\partial G_j} \delta G_j \quad (4)$$

[0074] where $\delta G_i = G_{i1} - G_1$ ($i=1, 2, \dots, m$) are the changes in the stiffness parameters, and the higher-order derivatives of K with respect to G_i vanish because K is assumed to be a linear function of G_i . Based on the finite element model, the global stiffness matrix of a distributed structure satisfies (4) as its higher-order derivatives with respect to each element stiffness parameter vanish.

[0075] Let the k -th eigenvalue and mass-normalized eigenvector of the damaged structure be related to λ^k and ϕ^k through

$$\lambda_i^k = \lambda^k + \sum_{j=1}^m \lambda_{(1)j}^k \delta G_j + \sum_{j=1}^m \lambda_{(2)j}^k \delta G_j \delta G_j + \dots + \sum_{j=1}^m \sum_{p=1}^{p-1} \dots \sum_{p-1}^m \lambda_{(p)j}^k \delta G_j \delta G_j \dots \delta G_j + e_{\lambda}^k \quad (5)$$

$$\phi_i^k = \phi^k + \sum_{j=1}^m \phi_{(1)j}^k \delta G_j + \sum_{j=1}^m \phi_{(2)j}^k \delta G_j \delta G_j + \dots + \sum_{j=1}^m \sum_{p=1}^{p-1} \dots \sum_{p-1}^m \phi_{(p)j}^k \delta G_j \delta G_j \dots \delta G_j + e_{\phi}^k \quad (6)$$

[0076] where $\lambda_{(1)j}^k, \lambda_{(2)j}^k, \dots$, and $\lambda_{(p)j}^k$ ($j=1, 2, \dots, m$) are the coefficients of the first, second, \dots , and p -th order perturbations for the eigenvalue, $\phi_{(1)j}^k, \phi_{(2)j}^k, \dots$, and $\phi_{(p)j}^k$ ($j=1, 2, \dots, m$) are the coefficient vectors of the first, second, \dots , and p -th order perturbations for the eigenvector, and e_{λ}^k and e_{ϕ}^k are the residuals of order $p+1$. Note that the numbers in the parentheses in the subscripts of the coefficients and coefficient vectors indicate the orders of the terms. By the Taylor expansion, one has for any $p \geq 1$,

$$\lambda_{(p)j}^k = \frac{\partial^p \lambda^k}{\partial G_j \partial G_j \dots \partial G_j} \quad \phi_{(p)j}^k = \frac{\partial^p \phi^k}{\partial G_j \partial G_j \dots \partial G_j} \quad (7)$$

[0077] By (7),

$$\lambda_{(p)j}^k \text{ and } \phi_{(p)j}^k$$

[0078] are symmetric in the p indices, i_j , . . . , and t. The right-hand sides of (7) are the p-th order sensitivities of the eigenvalues and eigenvectors with respect to the stiffness parameters.

[0079] Using the normalization relations of the eigenvectors, ϕ^k and ψ_j^k , and symmetry of the coefficient vectors in (6), as indicated earlier, one obtains

$$1 = (\phi_j^k)^T M \phi_j^k \quad (8)$$

$$= \left(\phi^k + \sum_{i=1}^m z_{i1}^k \delta G_i + \sum_{i=1}^m \sum_{j=1}^m z_{i2j}^k \delta G_i \delta G_j + \dots + \underbrace{\sum_{i=1}^m \sum_{j=1}^m \dots \sum_{p \text{ dimensions}}^m z_{ipij}^k \delta G_i \delta G_j \dots \delta G_i \delta G_j}_{p \text{ dimensions}} + \dots \right)^T$$

$$M \left(\phi^k + \sum_{i=1}^m z_{i1}^k \delta G_i + \sum_{i=1}^m \sum_{j=1}^m z_{i2j}^k \delta G_i \delta G_j + \dots + \underbrace{\sum_{i=1}^m \sum_{j=1}^m \dots \sum_{p \text{ dimensions}}^m z_{ipij}^k \delta G_i \delta G_j \dots \delta G_i \delta G_j}_{p \text{ dimensions}} + \dots \right) =$$

$$1 + \sum_{i=1}^m [(\phi^k)^T M z_{i1}^k + (z_{i1}^k)^T M \phi^k]$$

$$\delta G_i +$$

$$\sum_{i=1}^m \sum_{j=1}^m \frac{1}{R_{ij}^k} \{ 2 \mathbf{l}(\phi^k)^T M z_{i2j}^k + [(z_{i1}^k)^T M z_{i1}^k + (z_{i1}^k)^T M z_{i1}^k] + 2 \mathbf{l}(z_{i1}^k)^T M \phi^k \} \delta G_i \delta G_j +$$

$$\sum_{i=1}^m \sum_{j=1}^m \sum_{r=1}^m \frac{1}{R_{ijr}^k} \{ 3 \mathbf{l}(\phi^k)^T M z_{i3r}^k + 2 \mathbf{l}[(z_{i1}^k)^T M z_{i2j}^k + (z_{i1}^k)^T M z_{i2j}^k + (z_{i1}^k)^T M z_{i2j}^k] +$$

$$2 \mathbf{l}[(z_{i1}^k)^T M z_{i1}^k + (z_{i2j}^k)^T M z_{i1}^k + (z_{i2j}^k)^T M z_{i1}^k] + 3 \mathbf{l}(z_{i3r}^k)^T M \phi^k \} \delta G_i \delta G_j \delta G_r +$$

$$\dots + \underbrace{\sum_{i=1}^m \sum_{j=1}^m \dots \sum_{r=1}^m \frac{1}{R_{ijrst}^k} \{ p \mathbf{l}(\phi^k)^T M z_{ipst}^k - \mathbf{l} + (p-1)!}}_{p \text{ dimensions}}$$

$$\begin{aligned} & [(z_{i1}^k)^T M z_{i(p-1)t}^k - \mathbf{l} + (z_{i1}^k)^T M z_{i(p-1)t}^k - \mathbf{l} + \dots + (z_{i1}^k)^T M z_{i(p-1)t}^k - \mathbf{l}] + \\ & 2 \mathbf{l}(p-2)! [(z_{i2j}^k)^T M z_{i(p-2)t}^k - \mathbf{l} + (z_{i2j}^k)^T M z_{i(p-2)t}^k - \mathbf{l} + \dots + (z_{i2j}^k)^T M z_{i(p-2)t}^k - \mathbf{l}] + \dots + \\ & (p-2)! 2 \mathbf{l} [(z_{i(p-2)t}^k)^T M z_{i2j}^k + (z_{i(p-2)t}^k)^T M z_{i2j}^k + \dots + (z_{i(p-2)t}^k)^T M z_{i2j}^k] + \\ & (p-1)! [(z_{i(p-1)t}^k)^T M z_{i1}^k + (z_{i(p-1)t}^k)^T M z_{i1}^k + \dots + (z_{i(p-1)t}^k)^T M z_{i1}^k] + \\ & p \mathbf{l} [(z_{ipst}^k)^T M \phi^k \} \delta G_i \delta G_j \dots \delta G_i \delta G_r + \dots \end{aligned}$$

[0080] where the superscript T denotes transpose. For any p-th ($p \geq 1$) order term in the last expression of (8), the coefficient

$$R_{ij \rightarrow i}^p$$

[0081] is defined by

$$R_{ij \rightarrow i}^p = X_1!X_2! \cdots X_p!$$

[0082] where X_1, X_2, \dots , and X_p ($1 \leq \alpha \leq p$) are the numbers of the first, second, \dots , and last distinct indices within indices, i, j, \dots , and t , with $X_1 + X_2 + \dots + X_p = p$. For instance, $R_{1234} = 1!1!1!1! = 1$ with $a=4$, and $R_{112223} = 2!3!1! = 2!3!$ with $a=3$. Some explanations of the general p-th order term in the last expansion in (8) are in order. It includes p+1 types of terms ordered from the beginning to the end of the expression within the braces, with each type of terms except the first and last ones enclosed in square brackets. The c-th ($1 \leq c \leq p+1$) type of terms is obtained by multiplying a (c-1)-th order term in the expansion of $(\Phi_a^k)^T$ by a (p-c+1)-th order term in the expansion of $M\Phi_a^k$. For the c-th type of term, where $2 \leq c \leq p$, the p indices, i, j, \dots , and t are distributed in the subscripts of the two vectors pre- and post-multiplying M, whose numbers of indices in the subscripts are c-1 and p-c+1 respectively. For the first and last ((p+1)-th) types of terms, all the p indices lie in the subscripts of the vectors post- and pre-multiplying M, respectively. The number of terms within each set of square brackets equals the number of different combinations of indices in the subscripts of the vectors pre- and post-multiplying M. When all the p indices, i, j, \dots , and t , have distinct values, due to symmetry of these vectors in their indices, terms of the c-th ($1 \leq c \leq p+1$) type, involving different permutations of the same indices in the subscripts of the vectors, are equal and combined, resulting in the scaling factor (c-1)!(p-c+1)! in front of the square brackets. Consequently, the indices in the second through p-th summations range from the values of their preceding summation indices to m. When any of the p indices, i, j, \dots , and t , have equal values, the corresponding terms in each type are given by those in the previous case divided by

$$R_{ij \rightarrow i}^p$$

[0083] For instance, the 4th order term of the form $\delta G_i \delta G_j \delta G_k$ in the expansion of $(\Phi_a^k)^T M \Phi_a^k$ can be obtained from the expression for the p-th order term in (8):

$$\frac{1}{1!3!} \{ 4! (\delta^k)^T M_{c1222}^k + 3! (\delta_{c11}^k)^T M_{c2322}^k + (\delta_{c10}^k)^T M_{c3122}^k + (\delta_{c12}^k)^T M_{c20122}^k + (\delta_{c12}^k)^T M_{c23122}^k + 2!2! (\delta_{c212}^k)^T M_{c2222}^k + (\delta_{c202}^k)^T M_{c2222}^k +$$

-continued

$$\begin{aligned} & (\delta_{c202}^k)^T M_{c2222}^k + (\delta_{c222}^k)^T M_{c2012}^k + \\ & (\delta_{c202}^k)^T M_{c2012}^k + (\delta_{c222}^k)^T M_{c2012}^k + \\ & 3! (\delta_{c3222}^k)^T M_{c212}^k + (\delta_{c3122}^k)^T M_{c212}^k + \\ & (\delta_{c3122}^k)^T M_{c212}^k + (\delta_{c3122}^k)^T M_{c212}^k + \\ & 4! (\delta_{c41222}^k)^T M_{c1}^k \delta G_i \delta G_j^2 = \\ & \{ 4! (\delta^k)^T M_{c41222}^k + (\delta_{c411}^k)^T M_{c2322}^k + 3! (\delta_{c10}^k)^T M_{c3122}^k \} + \\ & 4! (\delta_{c2112}^k)^T M_{c2222}^k + (\delta_{c2022}^k)^T M_{c211}^k + \\ & 3! (\delta_{c3122}^k)^T M_{c212}^k + 4! (\delta_{c41222}^k)^T M_{c1}^k \delta G_i \delta G_j^2 \end{aligned}$$

[0084] where p=4 and the four indices involved, i, j, l , and o , are $i=1$ and $j=o=2$.

[0085] Equating the coefficients of the δG_i ($i=1, 2, \dots, m$) terms in (8) and using symmetry of the mass matrix yields

$$(\Phi^k)^T M_{c12}^k = 0 \quad (10)$$

[0086] Equating the coefficients of the $\delta G_i \delta G_j$ terms and using symmetry of M and $X_{(2)}^k$ yields

$$(\Phi^k)^T M_{c20}^k = -\frac{1}{2!} (\delta_{c11}^k)^T M_{c211}^k \quad (11)$$

[0087] for all $i, j=1, 2, \dots, m$. Following a similar procedure, one obtains

$$\begin{aligned} (\Phi^k)^T M_{c30}^k &= \\ & -\frac{2!}{3!} [(\delta_{c11}^k)^T M_{c230}^k + (\delta_{c11}^k)^T M_{c230}^k + (\delta_{c10}^k)^T M_{c230}^k] \end{aligned} \quad (12)$$

[0088] for $i, j, l=1, 2, \dots, m$. Equating the coefficients of the $\delta G_i \delta G_j \dots \delta G_l$ terms of p-th order in (8) yield

$$\begin{aligned} (\Phi^k)^T M_{cp0}^k \dots = & \\ & -\frac{1}{2!(p!)} \{ (p-1)! (\delta_{c11}^k)^T M_{c(p-1)0 \dots}^k + (\delta_{c11}^k)^T M_{c(p-1)0 \dots}^k + \\ & \dots + (\delta_{c10}^k)^T M_{c(p-1)0 \dots}^k \} + \\ & 2!(p-2)! (\delta_{c20}^k)^T M_{c(p-2)0 \dots}^k + (\delta_{c20}^k)^T M_{c(p-2)0 \dots}^k + \\ & \dots + (\delta_{c210}^k)^T M_{c(p-2)0 \dots}^k + \dots + \\ & (p-2)!2! (\delta_{c210}^k)^T M_{c(p-2)0 \dots}^k + (\delta_{c210}^k)^T M_{c(p-2)0 \dots}^k + \\ & \dots + (\delta_{c210}^k)^T M_{c(p-2)0 \dots}^k + \\ & (p-1)! (\delta_{c(p-1)0 \dots}^k)^T M_{c1}^k + (\delta_{c(p-1)0 \dots}^k)^T M_{c1}^k + \\ & \dots + (\delta_{c(p-1)0 \dots}^k)^T M_{c1}^k \} \end{aligned} \quad (13)$$

[0089] for $i, j, \dots, l=1, 2, \dots, m$. The p-1 types of terms, enclosed in the p-1 sets of square brackets on the right-hand side of (13), are ordered from the beginning to the end of the expression within the braces, and their structures are readily observed. When p is odd, by symmetry of

M and $\frac{\delta}{\zeta_{(p)j} \dots i}$, the $y - it \left(1 \leq y \leq \frac{p-j}{2} \right)$

[0090] type of terms is identical to the (p-y)-th type, and the two types of terms can be combined. Similarly, when p is even, the

$$y - it \left(1 \leq y \leq \frac{p}{2} - 1 \right)$$

[0091] type of terms equals and can be combined with the (p-y)-th type of terms. In this case, however, there is a separate type, the

$$\left(\frac{p}{2} \right) - it \text{ type,}$$

[0092] of terms in the middle of the expression.

[0093] Substituting (4)-(6) into (3) yields

$$\begin{aligned} & \left\{ K + \sum_{i=1}^m \frac{\partial K}{\partial G_i} \delta G_i \right\} \left\{ \phi^k + \sum_{i=1}^m \zeta_{1i}^k \delta G_i + \sum_{i=1}^m \sum_{j=1}^m \zeta_{2ij}^k \delta G_i \delta G_j + \dots \right\} = \\ & \sum_{i=1}^m \sum_{j=1}^m \sum_{k=1}^m \zeta_{3ijk}^k \delta G_i \delta G_j \delta G_k + \dots \Bigg\} = \\ & \left\{ \lambda^k + \sum_{i=1}^m \lambda_{1i}^k \delta G_i + \sum_{i=1}^m \sum_{j=1}^m \lambda_{2ij}^k \delta G_i \delta G_j + \right. \\ & \left. \sum_{i=1}^m \sum_{j=1}^m \sum_{k=1}^m \lambda_{3ijk}^k \delta G_i \delta G_j \delta G_k + \dots \right\} \\ & M \left\{ \phi^k + \sum_{i=1}^m \zeta_{1i}^k \delta G_i + \sum_{i=1}^m \sum_{j=1}^m \zeta_{2ij}^k \delta G_i \delta G_j + \right. \\ & \left. \sum_{i=1}^m \sum_{j=1}^m \sum_{k=1}^m \zeta_{3ijk}^k \delta G_i \delta G_j \delta G_k + \dots \right\} \end{aligned} \quad (14)$$

[0094] Equating the coefficients of the δG_i ($i=1, \dots, m$) terms in (14) yields

$$K_{\zeta_{1i}^k} + \frac{\partial K}{\partial G_i} \phi^k = \lambda^k M_{\zeta_{1i}^k} + \lambda_{1i}^k M \phi^k \quad (15)$$

[0095] Expanding ζ_{1i}^k using normalized eigenvectors of (1) as basis vectors, one has

$$\zeta_{1i}^k = \sum_{s=1}^N F_{(1)s}^k \phi^s \quad (16)$$

[0096] where

$$F_{(1)s}^k$$

[0097] is the coefficient of the u-th term and the number in the parentheses in its subscript corresponds to that of

$$\zeta_{1i}^k.$$

[0098] Pre-multiplying (15) by $(\phi^k)^T$ and using (1), (2), and (16) yields

$$\lambda_{1i}^k = (\phi^k)^T \frac{\partial K}{\partial G_i} \phi^k \quad (17)$$

[0099] Substituting (16) into (10) and using (2) yields

$$F_{(1)s}^k = 0 \quad (18)$$

[0100] Pre-multiplying (15) by $(\phi^k)^T$, where $1 \leq v \leq N$ and $v \neq k$, and using (1), (2), and (16) yields

$$F_{(1)s}^k = \frac{1}{N - \lambda^k} (\phi^k)^T \frac{\partial K}{\partial G_i} \phi^k \quad (19)$$

[0101] By (16), (18) and (19) we have determined

$$\zeta_{1i}^k.$$

[0102] Equating the coefficients of the $\delta G_i \delta G_j$ terms in (14) yields

$$2! K_{\zeta_{2ij}^k} + \frac{\partial K}{\partial G_i} \zeta_{1j}^k + \frac{\partial K}{\partial G_j} \zeta_{1i}^k = \quad (20)$$

$$2! \lambda^k M_{\zeta_{2ij}^k} + \lambda_{1i}^k M_{\zeta_{1j}^k} + \lambda_{1j}^k M_{\zeta_{1i}^k} + 2! \lambda_{2ij}^k M \phi^k$$

[0103] Expanding

$$\zeta_{2ij}^k$$

[0104] using normalized eigenvectors of (1) as basis vectors, one has

$$z_{2ij}^k = \sum_{s=1}^N P_{23ij}^k \phi^s \quad (21)$$

[0105] where

$$P_{23ij}^k$$

[0106] is the coefficient of the u-th term and the number in the parentheses in its subscript corresponds to that of

$$z_{2ij}^k.$$

[0107] Pre-multiplying (20) by $(\phi^k)^T$ and using (1), (2), (10), and (21) yields

$$\lambda_{2ij}^k = \frac{1}{2!} (\phi^k)^T \left[\frac{\partial K}{\partial G_i} z_{2ij}^k + \frac{\partial K}{\partial G_j} z_{2ij}^k \right] \quad (22)$$

[0108] Substituting (21) into (11) and using (2) yields

$$P_{23ij}^k = -\frac{1}{2!} (z_{2ij}^k)^T M_{23ij}^k \quad (23)$$

[0109] Pre-multiplying (20) by $(\phi^v)^T$, where $1 \leq v \leq N$ and $v \neq k$, and using (1), (2), and (21) yields

$$P_{23ij}^v = \frac{1}{2! (\lambda^k - \lambda^v)} (\phi^v)^T \left\{ \left[\frac{\partial K}{\partial G_i} z_{2ij}^k + \frac{\partial K}{\partial G_j} z_{2ij}^k \right] - [\lambda_{1ij}^k M_{23ij}^k + \lambda_{1ij}^v M_{23ij}^k] \right\} \quad (24)$$

[0110] By (21), (23) and (24) we have determined

$$z_{2ij}^k.$$

[0111] Equating the coefficients of the $\delta G_i \delta G_j \delta G_k$ terms in (14) yields

$$3! K z_{23ij}^k + 2! \left[\frac{\partial K}{\partial G_i} z_{2ij}^k + \frac{\partial K}{\partial G_j} z_{2ij}^k + \frac{\partial K}{\partial G_k} z_{2ij}^k \right] = 3! \lambda_{1ij}^k M_{23ij}^k + 2! [\lambda_{1ij}^k M_{23ij}^k + \lambda_{1ij}^v M_{23ij}^k + \lambda_{1ij}^v M_{23ij}^k] + \quad (25)$$

-continued

$$2! [\lambda_{1ij}^k M_{23ij}^k + \lambda_{1ij}^v M_{23ij}^k + \lambda_{1ij}^v M_{23ij}^k] + 3! \lambda_{1ij}^k M_{23ij}^k$$

[0112] Expanding

$$z_{2ij}^k$$

[0113] using normalized eigenvectors of (1) as basis vectors, one has

$$z_{2ij}^k = \sum_{s=1}^N P_{23ij}^k \phi^s \quad (26)$$

[0114] where

$$P_{23ij}^k$$

[0115] is the coefficient of the u-th term and the number in the parentheses in its subscript corresponds to that of

$$z_{2ij}^k.$$

[0116] Pre-multiplying (25) by $(\phi^k)^T$ and using (1), (2), (10), and (26) yields

$$\lambda_{1ij}^k = \frac{2!}{3!} (\phi^k)^T \left[\frac{\partial K}{\partial G_i} z_{2ij}^k + \frac{\partial K}{\partial G_j} z_{2ij}^k + \frac{\partial K}{\partial G_k} z_{2ij}^k - \lambda_{1ij}^k M_{23ij}^k - \lambda_{1ij}^v M_{23ij}^k - \lambda_{1ij}^v M_{23ij}^k \right] \quad (27)$$

[0117] Substituting (26) into (12) and using (2) yields

$$P_{23ij}^k = -\frac{2!}{3!} [(z_{2ij}^k)^T M_{23ij}^k + (z_{2ij}^k)^T M_{23ij}^k + (z_{2ij}^k)^T M_{23ij}^k] \quad (28)$$

[0118] Pre-multiplying (25) by $(\phi^v)^T$, where $1 \leq v \leq N$ and $v \neq k$, and using (1), (2), and (26) yields

$$P_{23ij}^v = \frac{2!}{3! (\lambda^k - \lambda^v)} (\phi^v)^T \left[\frac{\partial K}{\partial G_i} z_{2ij}^k + \frac{\partial K}{\partial G_j} z_{2ij}^k + \frac{\partial K}{\partial G_k} z_{2ij}^k - \lambda_{1ij}^k M_{23ij}^k - \lambda_{1ij}^v M_{23ij}^k - \lambda_{1ij}^v M_{23ij}^k \right] \quad (29)$$

[0119] By (26), (28) and (29) we have determined

$$z_{2ij}^k.$$

[0120] We proceed now to derive the perturbation solutions for the general p -th order terms in (5) and (6). Equating the coefficients of the $\delta G_1 \delta G_2 \dots \delta G_n \delta G_i$ terms of order p in (14) yields

$$\begin{aligned} p! K_{\alpha p \beta \dots \alpha}^{(p)} + (p-1)! \left[\frac{\partial K}{\partial G_1} \zeta_{\alpha(p-1)\beta \dots \alpha}^{(p)} + \frac{\partial K}{\partial G_2} \zeta_{\alpha(p-1)\beta \dots \alpha}^{(p)} + \dots + \right. \\ \left. \frac{\partial K}{\partial G_i} \zeta_{\alpha(p-1)\beta \dots \alpha}^{(p)} \right] \\ = p! K_{\alpha p \beta \dots \alpha}^{(p)} + (p-1)! [\lambda_{11}^{(p)} M_{\alpha(p-1)\beta \dots \alpha}^{(p)} + \\ \lambda_{11}^{(1)} M_{\alpha(p-1)\beta \dots \alpha}^{(p)} + \dots + \lambda_{11}^{(p)} M_{\alpha(p-1)\beta \dots \alpha}^{(p)}] + \\ 2!(p-2)! [\lambda_{21}^{(p)} M_{\alpha(p-2)\beta \dots \alpha}^{(p)} + \lambda_{21}^{(p)} M_{\alpha(p-2)\beta \dots \alpha}^{(p)} + \dots + \\ \lambda_{21}^{(p)} M_{\alpha(p-2)\beta \dots \alpha}^{(p)}] + \dots + p! K_{\alpha p \beta \dots \alpha}^{(p)} M_{\alpha p \beta \dots \alpha}^{(p)} \end{aligned} \quad (30)$$

[0121] Expanding

$$\zeta_{\alpha p \beta \dots \alpha}^{(p)}$$

[0122] using normalized eigenvectors of (1) as basis vectors, one has

$$\zeta_{\alpha p \beta \dots \alpha}^{(p)} = \sum_{n=1}^N P_{\alpha p \beta \dots \alpha}^{(p)} \phi_n^{(p)} \quad (31)$$

[0123] where

$$P_{\alpha p \beta \dots \alpha}^{(p)}$$

[0124] is the coefficient of the u -th term and the number in the parenthesis in its subscript corresponds to that of

$$\zeta_{\alpha p \beta \dots \alpha}^{(p)}$$

[0125] Pre-multiplying (30) by $(\phi^*)^T$ and using (1), (10), (31) and orthonormality relations of eigenvectors yields

$$\begin{aligned} \lambda_{\alpha p \beta \dots \alpha}^{(p)} = \frac{1}{p!} (\phi^*)^T [(p-1)! \left(\frac{\partial K}{\partial G_1} \zeta_{\alpha(p-1)\beta \dots \alpha}^{(p)} + \right. \\ \left. \frac{\partial K}{\partial G_2} \zeta_{\alpha(p-1)\beta \dots \alpha}^{(p)} + \dots + \frac{\partial K}{\partial G_i} \zeta_{\alpha(p-1)\beta \dots \alpha}^{(p)} \right) - \\ (p-1)! \lambda_{11}^{(p)} M_{\alpha(p-1)\beta \dots \alpha}^{(p)} + \lambda_{11}^{(1)} M_{\alpha(p-1)\beta \dots \alpha}^{(p)} + \dots + \\ \lambda_{11}^{(p)} M_{\alpha(p-1)\beta \dots \alpha}^{(p)}] - 2!(p-2)! \lambda_{21}^{(p)} M_{\alpha(p-2)\beta \dots \alpha}^{(p)} + \\ \lambda_{21}^{(1)} M_{\alpha(p-2)\beta \dots \alpha}^{(p)} + \dots + \lambda_{21}^{(p)} M_{\alpha(p-2)\beta \dots \alpha}^{(p)}] - \dots - \\ (p-2)! 2!(\lambda_{2p-2}^{(p)} M_{\alpha(p-2)\beta \dots \alpha}^{(p)} + \\ \lambda_{2p-2}^{(1)} M_{\alpha(p-2)\beta \dots \alpha}^{(p)} + \dots + \lambda_{2p-2}^{(p)} M_{\alpha(p-2)\beta \dots \alpha}^{(p)})] \end{aligned} \quad (32)$$

[0126] The p -th order sensitivities of eigenvalues are obtained from (7) and (32). They depend on the eigenvalue and eigenvector sensitivities of orders up to $p-2$ and $p-1$ respectively. Substituting (31) into (13) and using (2) yields

$$\begin{aligned} P_{\alpha p \beta \dots \alpha}^{(p)} = \\ \frac{1}{2(p!)} [(p-1)! (\lambda_{11}^{(p)} \bar{M}_{\alpha(p-1)\beta \dots \alpha}^{(p)} + (\lambda_{11}^{(1)} \bar{M}_{\alpha(p-1)\beta \dots \alpha}^{(p)} + \dots + \\ (\lambda_{11}^{(p)} \bar{M}_{\alpha(p-1)\beta \dots \alpha}^{(p)} + 2!(p-2)! (\lambda_{21}^{(p)} \bar{M}_{\alpha(p-2)\beta \dots \alpha}^{(p)} + \\ (\lambda_{21}^{(1)} \bar{M}_{\alpha(p-2)\beta \dots \alpha}^{(p)} + \dots + (\lambda_{21}^{(p)} \bar{M}_{\alpha(p-2)\beta \dots \alpha}^{(p)} + \dots + \\ (p-2)! 2!(\lambda_{2p-2}^{(p)} \bar{M}_{\alpha(p-2)\beta \dots \alpha}^{(p)} + (\lambda_{2p-2}^{(1)} \bar{M}_{\alpha(p-2)\beta \dots \alpha}^{(p)} + \dots + \\ (\lambda_{2p-2}^{(p)} \bar{M}_{\alpha(p-2)\beta \dots \alpha}^{(p)} + (p-1)! (\lambda_{2p-1}^{(p)} \bar{M}_{\alpha(p-1)\beta \dots \alpha}^{(p)} + \dots + \\ (\lambda_{2p-1}^{(1)} \bar{M}_{\alpha(p-1)\beta \dots \alpha}^{(p)} + \dots + (\lambda_{2p-1}^{(p)} \bar{M}_{\alpha(p-1)\beta \dots \alpha}^{(p)}))] \end{aligned} \quad (33)$$

[0127] Pre-multiplying (30) by $(\phi^*)^T$, where $1 \leq v \leq N$ and $v \neq k$, and using (1), (2), and (31) yields

$$\begin{aligned} P_{\alpha p \beta \dots \alpha}^{(p)} = \\ \frac{1}{p! (k - \lambda^k)} (\phi^*)^T [(p-1)! \left(\frac{\partial K}{\partial G_1} \zeta_{\alpha(p-1)\beta \dots \alpha}^{(p)} + \frac{\partial K}{\partial G_2} \zeta_{\alpha(p-1)\beta \dots \alpha}^{(p)} + \dots + \right. \\ \left. \frac{\partial K}{\partial G_i} \zeta_{\alpha(p-1)\beta \dots \alpha}^{(p)} \right) - (p-1)! \\ (\lambda_{11}^{(p)} M_{\alpha(p-1)\beta \dots \alpha}^{(p)} + \lambda_{11}^{(1)} M_{\alpha(p-1)\beta \dots \alpha}^{(p)} + \dots + \lambda_{11}^{(p)} M_{\alpha(p-1)\beta \dots \alpha}^{(p)} - \\ 2!(p-2)! (\lambda_{21}^{(p)} M_{\alpha(p-2)\beta \dots \alpha}^{(p)} + \lambda_{21}^{(1)} M_{\alpha(p-2)\beta \dots \alpha}^{(p)} + \dots + \\ \lambda_{21}^{(p)} M_{\alpha(p-2)\beta \dots \alpha}^{(p)} - \dots - (p-1)! (\lambda_{2p-1}^{(p)} M_{\alpha(p-1)\beta \dots \alpha}^{(p)} + \\ \lambda_{2p-1}^{(1)} M_{\alpha(p-1)\beta \dots \alpha}^{(p)} + \dots + \lambda_{2p-1}^{(p)} M_{\alpha(p-1)\beta \dots \alpha}^{(p)})] \end{aligned} \quad (34)$$

[0128] By (31), (33) and (34) we have determined

$$\zeta_{\alpha p \beta \dots \alpha}^{(p)}$$

[0129] The p -th order sensitivities of eigenvectors can be subsequently obtained from (7). They depend on the eigenvalue and eigenvector sensitivities of orders up to $p-1$.

[0130] Equations (5) and (6) serve both the forward and inverse problems. In the former one determines the changes in the eigenparameters with changes in the stiffness parameters. Damage detection is treated as an inverse problem, in which one identifies iteratively the changes in the stiffness parameters from a selected set of measured eigenparameters of the damaged structure: $\lambda_k^{(k)}$ ($k=1, 2, \dots, n_p$) and $\phi_k^{(k)}$ ($k=1, 2, \dots, n_p$), where $1 \leq n_p$, $n_p \leq N$. Here $\lambda_k^{(k)}$ and $\phi_k^{(k)}$ are assumed to be the perfect eigenparameters; simulated noise is included in the measured eigenparameters in the beam and frame examples that follow. Often we choose a set of n measured eigenparameter pairs to detect damage, i.e., $n_p = n_p = n$. Let the number of the measured degrees of freedom of $\phi_k^{(k)}$ be N_m , $N_m = N$ and $N_m < N$ when we have complete and incomplete eigenvector measurements, respectively. With reduced measurements the unmeasured degrees of freedom of $\phi_k^{(k)}$ is estimated first using a modified

eigenvector expansion method (see the beam and frame examples below) and ϕ_a^k is mass-normalized subsequently. Only the component equations corresponding to the measured degrees of freedom of ϕ_a^k are used in (6). The system equations in Eqs. (5) and (6) involves $n_a + n_b N_m$ scalar equations with m unknowns, which are in general determinate if $n_a + n_b N_m = m$, under-determined if $n_a + n_b N_m < m$, and over-determined if $n_a + n_b N_m > m$. In the first iteration, λ^k and ϕ^k in (5) and (6) correspond to the eigenparameters of the structure with the initial stiffness parameters $G_i^{(0)}$. With the perturbation terms determined as shown above, the changes in the stiffness parameters $\delta G_i^{(1)}$, where the number in the superscript denotes the iteration number, can be solved from (5) and (6) using an optimization method discussed below. The estimated stiffness parameters of the damaged structure are updated by $G_i^{(1)} = G_i^{(0)} + \delta G_i^{(1)}$. With the updated stiffness parameters, the eigenparameters, λ^k and ϕ^k , in (5) and (6) are re-calculated from the eigenvalue problem (1) and the perturbation terms are re-evaluated. One subsequently finds $\delta G_i^{(2)}$ using the same method as that in the first iteration. This process is continued until the termination criterion, $|\delta G_i^{(L)}| < \epsilon$, where L is the last iteration number and ϵ is some small constant, is satisfied for all $i=1, 2, \dots, m$. Note that after the w -th ($1 \leq w < L$) iteration, we set $G_i^{(w)}$ to G_{hi} if $G_i^{(w)} > G_{hi}$, and to zero or some small stiffness value ϵ_G if $G_i^{(w)} < 0$. A flowchart for the iterative algorithm is shown in FIG. 1B. When a single iteration is used, the iterative method becomes a direct method.

[0131] FIG. 1B shows steps included in a method for detecting structural damage in accordance with one embodiment of the present invention. The method includes as an initial step measuring one or more eigenparameters, λ_a^k , ϕ_a^k (Block 1). These eigenparameters are then compared with estimated eigenparameters associated with the stiffness parameters, $G_i^{(0)}$ (Block 2). The differences between the measured and estimated eigenparameters are then used by the perturbation method to establish system equations (5) and (6) (Block 3). The perturbation method may be a first or higher order multiple-parameter perturbation procedure.

[0132] Next, an optimization method may be used to find the changes in the stiffness parameters $\delta G_i^{(w)}$ (Block 4). These values are then compared to the predetermined value ϵ (Block 5), and if the absolute values are less than ϵ the stiffness parameters identified are set as $G_i^{(w-1)}$ (Block 6).

[0133] If the absolute values are not all less than ϵ , the process proceeds along an iterative path where the stiffness parameters are first updated (Block 7). The stiffness parameters are then bounded between 0 or ϵ_G and G_{hi} (Block 8), and eigenparameters associated with the updated stiffness parameters are calculated (Block 9). The comparison of Block 2 is then performed based on these calculated, or estimated, eigenparameters.

[0134] Optimization Methods

[0135] Neglecting the residuals of order $p+1$ in (5) and (6) yields a system of polynomial equations of order p . When $n_a + n_b N_m \leq m$, $\delta G_i^{(w)}$ ($i=1, 2, \dots, m$) at the w -th iteration can be solved from the resulting equations. There are generally an infinite number of solutions when $n_a + n_b N_m < m$, a unique solution when $n_a + n_b N_m = m$ and $p=1$, and a finite number of solutions when $n_a + n_b N_m = m$ and $p>1$. When $n_a + n_b N_m > m$, one generally cannot find $\delta G_i^{(w)}$ to satisfy all the equations, and an optimization method can be used to find $\delta G_i^{(w)}$ which

minimize an objective function related to the errors in satisfying these equations. We use here the same notations, e_{λ}^k and e_{ϕ}^k , to denote the errors in satisfying the system equations in (5) and (6) respectively. Consider the objective function

$$J = \sum_{k=1}^{n_\lambda} W_{\lambda}^k (e_{\lambda}^k)^2 + \sum_{k=1}^{n_\phi} W_{\phi}^k (e_{\phi}^k)^2 \quad (35)$$

[0136] where W_{λ}^k ($k=1, 2, \dots, n_\lambda$) and W_{ϕ}^k ($k=1, 2, \dots, n_\phi$) are the weighting factors, and J is a function of $\delta G_i^{(w)}$ when one substitutes the expressions for e_{λ}^k and e_{ϕ}^k in (5) and (6) into (35). When the first-order perturbations are retained in (5) and (6), the least-squares method can be used to determine $\delta G_i^{(w)}$ which minimize (35) with $W_{\lambda}^k = W_{\phi}^k = 1$. Other weighting factors can be handled by dividing (5) and (6) by

$$\frac{1}{\sqrt{W_{\lambda}^k}} \quad \text{and} \quad \frac{1}{\sqrt{W_{\phi}^k}}$$

[0137] respectively. The method determines essentially the generalized inverse of the resulting system matrix, and is also known as the generalized inverse method. When the perturbations up to the p -th ($p \geq 1$) order are included in (5) and (6), the gradient and quasi-Newton methods [25] can be used to determine $\delta G_i^{(w)}$ iteratively. Unlike the generalized inverse method, the methods are applicable when other objective functions are defined. While the optimization methods are introduced for over-determined systems, they can be used when $n_a + n_b N_m \leq m$, in which case $J=0$ (i.e., $e_{\lambda} = e_{\phi} = 0$) when the optimal solutions are reached.

[0138] Gradient Method

[0139] To minimize the objective function in (35) at the w -th iteration, one can use the algorithm

$$\delta G_{[p]}^{[w]} = \delta G_{[p-1]}^{[w]} - \alpha_p f_{p-1} \quad (36)$$

[0140] to update the changes in the stiffness parameters, where

$$\delta G_{[p]}^{[w]} = (\delta G_{[1]}^{[w]}, \delta G_{[2]}^{[w]}, \dots, \delta G_{[m]}^{[w]})^T,$$

[0141] $\alpha_p > 0$ is the step size, and f_{p-1} equals the gradient vector

$$f_{p-1} = \left(\frac{\partial J}{\partial G_1^{[w]}}, \frac{\partial J}{\partial G_2^{[w]}}, \dots, \frac{\partial J}{\partial G_m^{[w]}} \right)^T$$

[0142] associated with

$$\delta G_{(b-1)}^{(n)},$$

[0143] Note that the subscript b ($b \geq 1$) in all the variables in (36) denotes the number of nested iterations. The initial values used are

$$\delta G_{(0)}^{(n)} = 0,$$

[0144] The nested iteration is terminated when $\alpha_b \|g_b\|_{\infty} \leq \gamma$, where $\|\cdot\|_{\infty}$ is the infinity norm and γ is some small constant, or the number of nested iterations exceeds an acceptable number, D.

[0145] Quasi-Newton Methods

[0146] Due to its successive linear approximations to the objective function, the gradient method can progress slowly when approaching a stationary point. The quasi-Newton methods can provide a remedy to the problem by using essentially quadratic approximations to the objective function near the stationary point. The iteration scheme of these methods is given by (36) with $f_{b-1} = B_{b-1} g_{b-1}$, where B_{b-1} is an approximation to the inverse of the Hessian matrix used at the b-th nested iteration, and the other variables the same as those previously discussed. Initially, we set

$$\delta G_{(0)}^{(n)} = 0$$

[0147] and $B_0 = I$, the identity matrix. The matrix B_b is updated using either the DFP formula

$$B_b = B_{b-1} + \frac{(\delta G_{(b)}^{(n)} - \delta G_{(b-1)}^{(n)}) (\delta G_{(b-1)}^{(n)} - \delta G_{(b-1)}^{(n)})^T}{(\delta G_{(b)}^{(n)} - \delta G_{(b-1)}^{(n)})^T (g_b - g_{b-1})} - \frac{[B_{b-1} (g_b - g_{b-1})] [B_{b-1} (g_b - g_{b-1})]^T}{(g_b - g_{b-1})^T B_{b-1} (g_b - g_{b-1})} \quad (37)$$

[0148] or the BFGS formula

$$B_b = B_{b-1} + \left[1 + \frac{(g_b - g_{b-1})^T B_{b-1} (g_b - g_{b-1})}{(\delta G_{(b)}^{(n)} - \delta G_{(b-1)}^{(n)})^T (g_b - g_{b-1})} \right] \frac{(\delta G_{(b)}^{(n)} - \delta G_{(b-1)}^{(n)}) (\delta G_{(b-1)}^{(n)} - \delta G_{(b-1)}^{(n)})^T}{(\delta G_{(b)}^{(n)} - \delta G_{(b-1)}^{(n)})^T (g_b - g_{b-1})} - \frac{B_{b-1} (g_b - g_{b-1}) (g_b - g_{b-1})^T B_{b-1}}{[(\delta G_{(b)}^{(n)} - \delta G_{(b-1)}^{(n)})^T (g_b - g_{b-1})]} \quad (38)$$

[0149] The nested iteration is terminated when $\alpha_b \|B_{b-1} g_b\|_{\infty} \leq \gamma$ or the number of iterations exceeds D. A flowchart for

the quasi-Newton methods, including the step size search procedure as outlined below, is shown in FIG. 2.

[0150] Step Size Search Procedure

[0151] The optimal step size for the gradient and quasi-Newton methods is determined in each nested iteration to minimize the function

$$J(\delta G_{(b-1)}^{(n)} - \alpha_b f_{b-1}) = F(\alpha_b)$$

[0152] with respect to α_b . The search procedure is divided into two phases: an initial search to bracket the optimum α_b^* , and a golden section search to locate α_b^* within the bracket, as shown in FIG. 2.

[0153] Initial Bracketing. Choose the starting point $x_1 = 0$ and an initial increment $\Delta > 0$. Let $x_2 = x_1 + \Delta$, $F_1 = F(x_1)$, and $F_2 = F(x_2)$. Since for the gradient and quasi-Newton methods, $f_0 = g_0$ and it is along a descent direction of J when Δ is sufficiently small, one has $F_2 < F_1$. Rename 2Δ as Δ , and let $x_3 = x_2 + \Delta$ and $F_3 = F(x_3)$. If $F_3 > F_2$, stop and α_b^* is contained in the interval (x_1, x_3) . Otherwise, rename x_2 as x_1 and x_3 as x_2 , then F_2 becomes F_1 and F_3 becomes F_2 . Rename 2Δ as Δ , and let $x_3 = x_2 + \Delta$ and $F_3 = F(x_3)$. Compare F_3 and F_2 , and repeat the above procedure if $F_3 < F_2$ until $F_3 > F_2$, with the final interval (x_1, x_3) containing α_b^* .

[0154] Golden Section Search. If $|x_3 - x_1| > |x_2 - x_1|$, define a new point:

$$x_4 = x_1 + 0.382(x_3 - x_1) \quad (39)$$

[0155] Otherwise, rename x_1 as x_3 and x_3 as x_1 , and then define x_4 using (40). Let $F_4 = F(x_4)$. If $F_4 < F_3$, rename x_4 as x_2 , then F_4 becomes F_3 . Otherwise, rename x_2 as x_1 and x_4 as x_2 , then F_3 becomes F_1 and F_4 becomes F_2 . Compare $|x_2 - x_1|$ and $|x_3 - x_1|$, and repeat the above procedure until $|x_3 - x_1| \leq \epsilon_a$, where ϵ_a is some small constant. Then choose

$$\alpha_b^* = \frac{x_1 + x_2}{2}.$$

MASS-SPRING SYSTEM EXAMPLE

[0156] The algorithm discussed above is used to identify the stiffness parameters of a N-degree-of-freedom system consisting of a serial chain of masses and springs, such as the system shown in FIG. 3. Let the masses of the system be $M_i = 1$ kg ($i=1, 2, \dots, N$), and the stiffnesses of the undamaged springs be $G_{i0} = 1$ N/m ($i=1, 2, \dots, m$), where $m=N+1$. The system is said to have a small, medium and large level of damage if the maximum reduction in the stiffnesses is within 30%, between 30 and 70%, and over 70%, respectively. The mass matrix M is an $N \times N$ identity matrix, and the stiffness matrix K is a banded matrix with entries $K_{ii} = G_i + G_{i+1}$ ($i=1, 2, \dots, N$), $K_{i(i+1)} = K_{(i+1)i} = -G_{i+1}$ ($i=1, 2, \dots, N-1$), and all other entries equal to zero. The matrices

$$\frac{\partial K}{\partial G_i} \text{ and } \frac{\partial K}{\partial G_N}$$

[0157] have a unit value in entries (1, 1) and (N, N), respectively, and zero entries elsewhere. The nonzero entries of the matrices

$$\begin{aligned} \frac{\partial K}{\partial G_i} \quad (i=2, 3, \dots, N-1) \text{ are} \\ \left(\frac{\partial K}{\partial G_i} \right)_{(i-1)(i-1)} = \left(\frac{\partial K}{\partial G_i} \right)_{ii} = 1 \text{ and} \\ \left(\frac{\partial K}{\partial G_i} \right)_{i(i-1)} = \left(\frac{\partial K}{\partial G_i} \right)_{(i-1)i} = -1. \end{aligned}$$

[0158] We look at a forward problem first with $N=3$ and $m=4$. The stiffnesses of the damaged system are $G_{11}=G_{22}=1\text{N/m}$, $G_{33}=0.3\text{N/m}$ and $G_{12}=0\text{N/m}$. The undamaged system is considered as the unperturbed system and the damaged system as the perturbed system. Based on the eigenparameters of the undamaged system, the eigensolutions of the damaged system are obtained using the first-, second-, and third-order perturbations, as shown in Table 1 below. The results show that even with the large changes in stiffness, the third-order perturbation solutions compare favorably with the exact solutions for the damaged system. The higher-order perturbation solutions can be used for large order systems when their direct eigensolutions become costly.

TABLE 1

Eigenparameters	Bigenvalues of the damaged system from an eigenvalue problem solver (exact) and perturbation analysis				
	Exact	Unperturbed	Perturbed		
			1st order	2nd order	3rd order
λ^1	0.10602	0.58579	0.30576	0.15670	0.10090
λ^2	1.27538	2.00000	1.15000	1.25500	1.29344
λ^3	2.21859	3.41421	2.14424	2.18830	2.20567
ϕ^1	$\begin{Bmatrix} 0.16516 \\ 0.65733 \\ 0.73528 \end{Bmatrix}$	$\begin{Bmatrix} 0.50000 \\ 0.70711 \\ 0.50000 \end{Bmatrix}$	$\begin{Bmatrix} 0.28523 \\ 0.68836 \\ 0.74129 \end{Bmatrix}$	$\begin{Bmatrix} 0.16111 \\ 0.66444 \\ 0.79452 \end{Bmatrix}$	$\begin{Bmatrix} 0.12907 \\ 0.65040 \\ 0.76653 \end{Bmatrix}$
ϕ^2	$\begin{Bmatrix} 0.95541 \\ 0.07840 \\ -0.28470 \end{Bmatrix}$	$\begin{Bmatrix} 0.70711 \\ -0.00000 \\ -0.70711 \end{Bmatrix}$	$\begin{Bmatrix} 0.95459 \\ 0.10607 \\ -0.45962 \end{Bmatrix}$	$\begin{Bmatrix} 0.00188 \\ 0.14319 \\ -0.31776 \end{Bmatrix}$	$\begin{Bmatrix} 0.97976 \\ 0.12310 \\ -0.26810 \end{Bmatrix}$
ϕ^3	$\begin{Bmatrix} 0.24478 \\ -0.74952 \\ 0.61507 \end{Bmatrix}$	$\begin{Bmatrix} 0.50000 \\ -0.70711 \\ 0.50000 \end{Bmatrix}$	$\begin{Bmatrix} 0.36477 \\ -0.72586 \\ 0.60871 \end{Bmatrix}$	$\begin{Bmatrix} 0.29635 \\ -0.74132 \\ 0.62482 \end{Bmatrix}$	$\begin{Bmatrix} 0.26445 \\ -0.74875 \\ 0.62362 \end{Bmatrix}$

[0159] Consider now the damage detection problem with $N=9$, $m=10$, $G_{13}=0.5\text{N/m}$, $G_{23}=0.7\text{N/m}$, $G_{110}=0.8\text{N/m}$ and $G_{ii}=1\text{N/m}$ ($i=1, 2, 3, 4, 6, 7, 9$). We set $W_{\lambda}^k = W_{\phi}^k = 1$, $\epsilon=0.001$, $\gamma=10^{-10}$, σ_{i-1} for all i , and $D=500$; the actual numbers of nested iterations in all the cases are much smaller than D .

Since vanishing stiffness in any spring other than the two end ones in FIG. 1 can result in two decoupled subsystems, when $G_i^{(w)} < 0$ we set $G_i^{(w)} = \epsilon_c = 0.1\text{N/m}$ in the first two iterations and to 0.1N/m in the remaining iterations for all the cases considered here. A relatively large value is assigned to ϵ_c in the initial iterations to avoid close eigenvalues in the mass-spring system and small denominators in (19). This improves convergence especially when a small number of eigenparameter pairs are used. A smaller value is used for ϵ_c in the later iterations to improve the accuracy of stiffness estimation when there is a large level of stiffness reduction. Using the first-order perturbations and different numbers of eigenparameter pairs, the maximum errors in estimating the stiffnesses of the damaged system at the w -th iteration, defined by

$$E = \max_{1 \leq i \leq N} \frac{|G_i^{(w)} - G_{di}|}{G_{di}} \quad (40)$$

[0160] are shown in FIGS. 4A and 4B for all the iterations. In FIG. 4A $p=1$ and $n=1, 2, 3$, and in FIG. 4B $p=1$ and $n=4, 5, \dots, 9$. When $n=1$, the error decreases slowly, though monotonically, and there is an estimation error of 1.5% at the end of iteration. While the errors can increase with the iteration number before approaching zero for $n=3$, they decrease monotonically for $n=2$ and $n \geq 4$. All the stiffnesses are exactly identified at the end of iteration when $n \geq 2$. Note that the number of the system equations equals and exceeds the number of unknowns when $n=1$ and $n \geq 2$, respectively. Since the system equations are linear, they have a unique

solution when $n=1$, and J has a unique minimum when $n \geq 2$. With the small γ the gradient method and the quasi-Newton methods using the DFP and BFGS formulas yield exactly the same results as the generalized inverse method (not shown here). Because the generalized inverse method does not

involve any nested iteration, it is the most efficient one among the four methods. While not shown here, the results indicated that the quasi-Newton methods converge faster than the gradient method and the BFGS method has the similar performance to the DFP method. In what follows the BFGS method will be used with the higher-order perturbations. With the second-order perturbations the errors shown in FIG. 4C decrease monotonically for all n ($n=1, 2, \dots, 9$). The errors at $w=1$ in the expanded view decrease in the order $n=3, 2, 4, 9, 7, 8$, with the lines for $n=5$ and 7 virtually indistinguishable. In FIG. 4(A-C) the following symbols are used for different n : \rightarrow 407 $n=1$; \rightarrow 2 $n=2$; \rightarrow 3 $n=3$; \rightarrow 4 $n=4$; \rightarrow 5 $n=5$; \rightarrow 6 $n=6$; \rightarrow 7 $n=7$; \rightarrow 8 $n=8$; \rightarrow 9 $n=9$. While the use of the second-order perturbations improves the accuracy of stiffness estimation in each iteration and reduces the number of iterations, it takes a much longer time to compute the higher-order perturbations and the associated optimal solutions.

[0161] When only the first few eigenvalues are used, for instance, $n_3=5$ and $n_0=0$, the stiffnesses identified with the first-order perturbations,

$$G^{(0)} = (0.875, 0.976, 0.926, 0.864, 0.699, 0.699, 0.864, 0.926, 0.976, 0.875)^T \text{ N/m} \quad (41)$$

[0162] where the number in the superscript denotes the last iteration number, correspond to those of a different system with the same eigenvalues for the first five modes as the damaged system. The same stiffnesses are identified with the second-order perturbations. Similarly, when the first eigenvector is used, i.e., $n_0=1$ and $n_3=0$, the stiffnesses identified with the first-order perturbations are those of a different system with the same eigenvector for the first mode as the damaged system:

$$G^{(0)} = (0.989, 0.991, 0.995, 1, 0.520, 0.829, 0.940, 0.668, 0.959, 0.768)^T \text{ N/m} \quad (42)$$

[0163] With the second-order perturbations the stiffnesses of the damaged system are identified. The stiffnesses identified are not unique because the system equations in each iteration are under-determined. The solution given by the generalized inverse method here in each iteration is the minimum norm solution. Increasing the number of eigenparameters used can avoid this problem.

[0164] If the system has a large level of damage, i.e., $G_{15}=0.3$ N/m, $G_{410}=0.1$ N/m, with the other parameters unchanged, the stiffnesses of the damaged system are identified with the first-order perturbations after 55 iterations when $n=1$ and 6 iterations when $n=2$ and 3 as shown in FIG. 5A. For $n=4, 5, 6, 7$, the errors decrease monotonically and the number of iterations is reduced slightly, as shown in FIG. 5B, which has an expanded view near $w=1$. With the second-order perturbations the errors shown in FIG. 5C decrease monotonically for $n=1, 2, \dots, 5$, and the number of iteration for $n=1$ is reduced from 55 in FIG. 5A to 4. The errors at $w=1$ in the expanded view in FIG. 5C decrease in the order $n=3, 2, 4, 5$, with the lines for $n=2$ and 4 virtually indistinguishable. The symbols used in FIG. 5A-C for $n=1, 2, \dots, 7$ are the same as those in FIG. 4A-C.

[0165] Finally, consider a large order system with a large level of damage: $N=39$, $m=40$, $G_{415}=0.7$ N/m, $G_{410}=G_{437}=0.1$ N/m, $G_{425}=0.8$ N/m, $G_{411}=1$ N/m ($1 \leq i \leq 40$ and $i \neq 12, 19, 28, 37$), and the other parameters are the same as those in the previous example. With the first-order perturbations the exact stiffnesses are identified after 57 iterations when $n=1$,

as shown FIG. 6A. Using a larger number of eigenparameter pairs ($n=2, 3, 4, 5$) significantly reduces the number of iterations, as shown in FIG. 6B. The errors at $w=2$ in the expanded view in FIG. 6B decrease in the order $n=4, 2, 3, 5$. With the second-order perturbations the exact stiffnesses are identified after 6 iterations when $n=1$ and 3 iterations when $n=2$, as shown in FIG. 6C, which has an expanded view for $1 \leq w \leq 4$. The symbols used in FIG. 6(A-C) for $n=1, 2, \dots, 5$ are the same as those in FIGS. 4A-C and 5A-C.

FIXED-FIXED BEAM EXAMPLE

[0166] The algorithm discussed above may be applied to detecting structural damage in an aluminum beam with fixed boundaries. The beam of length $L_0=0.7$ m, width $W=0.0254$ m, and thickness $H=0.0031$ m has an area moment of inertia

$$I = \frac{1}{12} WH^3 = 6.3058 \times 10^{-11} \text{ m}^4$$

[0167] and a mass density $\rho=2715$ kg/m³. The finite element method is used to model the its transverse vibration. The beam is divided into N_e elements, as shown in FIG. 7, with the length of each element being

$$L_e = \frac{L_0}{N_e}$$

[0168] There are N_e+1 nodes. With V_i and θ_i denoting the translational and rotational displacements at node i ($i=1, 2, \dots, N_e+1$), the displacement vector of the i -th ($i=1, 2, \dots, N_e$) element is $[V_{i0}, V_{i1}, \theta_{i1}]^T$. The Young's modulus is assumed to be constant over each beam element and that of the i -th element is denoted by G_i . The Young's modulus of the undamaged beam is $G_0=69 \times 10^9$ N/m². Hence $G_{i0}=G_0$ for $i=1, 2, \dots, m$, where $m=N_e$. Small to large levels of damage correspond to reductions of the moduli defined for the Mass-Spring Example. The mass and stiffness matrices of the i -th beam element are

$$M_i^e = \frac{\rho W H L_e}{420} \begin{bmatrix} 156 & -22L_e & 54 & 13L_e \\ -22L_e & 4L_e^2 & -13L_e & -3L_e^2 \\ 54 & -13L_e & 156 & 22L_e \\ 13L_e & -3L_e^2 & 22L_e & 4L_e^2 \end{bmatrix}, \quad (43)$$

$$K_i^e = \frac{G_i I}{L_e} \begin{bmatrix} 12 & 6L_e & -12 & 6L_e \\ 6L_e & 4L_e^2 & -6L_e & 2L_e^2 \\ -12 & -6L_e & 12 & -6L_e \\ 6L_e & 2L_e^2 & -6L_e & 4L_e^2 \end{bmatrix}$$

[0169] Using the standard assembly process yields the $2(N_e+1) \times 2(N_e+1)$ global mass and stiffness matrices. Constraining the translational and rotational displacements of the two nodes at the boundaries to zero yields the $N \times N$ M and K matrices, where $N=2(N_e-1)$ is the degrees of freedom of the system. The displacement vector of the system, involving the displacements of the 2^{nd} through N_e -th node, is $[V_{20}, V_{21}, V_{30}, V_{31}, \dots, V_{N_e}, \theta_{N_e}]^T$. The matrix

$$\frac{\partial K}{\partial G_i}$$

[0170] ($i=1, 2, \dots, m$) can be obtained from K by setting G_{i-1} and $G_{i+1} = \dots = G_{m-1} = G_{m+1} = \dots = G_m = 0$. The parameters $W_{\lambda_i}^k$, $W_{\phi_i}^k$, ϵ_i , γ_i , C_i and D are set to the same values as those previously discussed, and ϵ_{G_i} is set to 0.15 G_{i0} in the first two iterations and to 0.05 G_{i0} in the remaining iterations. The first-order perturbations are used unless indicated otherwise.

[0171] Consider first the cases with $N_m=m=10$ and $N=18$. When the system has a medium level of damage:

$$G_{i0}=(1, 1, 1, 1, 0.5, 1.1, 0.7, 1, 0.8)^T \times G_0 \quad (44)$$

[0172] the stiffness parameters of the damaged system are identified after 6 iterations with $n=1$. When the system has a large level of damage:

$$G_{i0}=(1, 1, 1, 1, 0.3, 1, 1, 0.7, 1, 0.1)^T \times G_0 \quad (45)$$

[0173] the stiffness parameters of the damaged system are identified after 7 iterations with $n=1$. Consider next the cases with $N_m=20, 40$ and 80 . For the systems with medium and large levels of damage, the stiffness parameters of the first 10 elements are given by (44) and (45), respectively, and those of the remaining elements are G_{i0} . In all the cases the stiffness parameters of the damaged systems are identified within 10 iterations when $n=1$. The numbers of iterations are reduced slightly when the second-order perturbations are used. Note that the system equations are over-determined when $n=1$.

[0174] When only the translational degrees of freedom of an eigenvector are measured, a modified eigenvector expansion method is used to estimate the unmeasured rotational degrees of freedom. To this end, ϕ_d^k is partitioned in the form $\phi_d^k = [(\phi_{dm}^k)^T, (\phi_{dn}^k)^T]^T$, where ϕ_{dm}^k and ϕ_{dn}^k are the measured and unmeasured degrees of freedom of ϕ_d^k , respectively. Similarly, ϕ^k in (6) is partitioned in the form $\phi^k = [(\phi_m^k)^T, (\phi_n^k)^T]^T$, where ϕ_m^k and ϕ_n^k correspond to the measured and unmeasured components of ϕ^k , respectively. Since ϕ_{dm}^k , ϕ_m^k and ϕ_{dn}^k are known in each iteration, ϕ_{dn}^k is estimated from $\phi_{dn}^k = k[(\phi_m^k)^T \phi_{dm}^k] \phi_n^k$, where the superscript \dagger denotes generalized inverse. Once the rotational degrees of freedom of ϕ_d^k are determined, ϕ_d^k and ϕ^k are converted to their original forms and ϕ_d^k is mass-normalized. Only the component equations corresponding to the measured degrees of freedom of ϕ_d^k are used in (6) and the system equations are determinate when $n=1$. The exact stiffness parameters of the damaged systems considered above can be identified. For the 10- and 20-element beams with the medium levels of damage, the stiffness parameters are identified after 6 and 24 iterations, respectively, when $n_1=1$ and $n_2=2$. For the 10- and 20-element beams with the large levels of damage, the stiffness parameters are identified after 9 iterations when $n_1=1$ and $n_2=3$ and 10 iterations when $n_2=2$, respectively.

[0175] Finally, the effects of measurement noise on the performance of the algorithm are evaluated for the 10-element beam with the large level of damage. Simulated noise is included in the measured eigenparameters:

$$\lambda_i^k = \lambda_i^k + v R_i^k, \lambda_i^k, \phi_i^k = \phi_i^k + v R_i^k \phi_i^k \quad (46)$$

[0176] where λ_i^k and ϕ_i^k are the k -th perfect eigenvalue and eigenvector, respectively, R_i^k is a uniformly distributed random variable in the interval $[-1, 1]$, R_i^k is a diagonal matrix whose diagonal entries are independently, uniformly distributed random variables in the interval $[-1, 1]$, and $v \in [0, 1]$ is the noise level. Note that R_i^k and R_i^k are generated for each measured mode. Each random parameter is generated 10 times and the average is used. Three different noise levels are considered: $v=5\%$, 10% and 20% . When all the degrees of freedom of an eigenvector are measured, the stiffness parameters identified with $n=1, 2$, and 3 are shown in FIGS. 8A, 8B, and 8C, respectively. The following symbols are used for different noise levels: \square , $v=5\%$; \square , $v=10\%$; \square , $v=20\%$. When only the translational degrees of freedom of an eigenvector are measured, the eigenvector expansion method described above is used and the stiffness parameters identified with $n=2$ and $n=3$ are shown in FIGS. 9A and 9B, respectively. The same symbols as those in FIGS. 8A-C are used in FIG. 9A-B for different noise levels. The stiffness parameters corresponding to $v=0$ in FIGS. 8 and 9 are the exact values. It is seen that in the presence of noise, the stiffness parameters can be accurately identified with an increased number of measured eigenparameters.

[0177] Space Frame Example

[0178] The damage detection method can be applied to more complex structures, such as, for example, the modular, four bay space frame shown in FIG. 10. In this example and all the following examples the first order perturbation approach along with the generalized inverse method is used. The four-bay space frame example shown in FIG. 10 is made of extruded aluminum with 48 members, and is 8' tall, 1.46' wide and 1.8' deep. The horizontal and diagonal members have the same cross-sectional dimensions (25.4 mm \times 12.7 mm) and the vertical members are "L"-angles with cross-sectional dimensions 50.8 mm \times 50.8 mm \times 6.35 mm (thickness). All the members are connected through bolted joints. The frame is assumed to be fixed to the ground. The finite element method is used to model the 3-dimensional vibration of the frame, with each member modeled with four 12-degrees-of-freedom beam elements. The total degrees of freedom are 960 when the boundary conditions are applied. The Young's modulus is assumed to be constant over each member and that of the i -th ($1 \leq i \leq m=48$) member is denoted by G_i . The Young's modulus of the undamaged member is $G_0=69 \times 10^9$ N/m² and $G_{i0}=G_0$. A vertical (member 1) and a diagonal (member 48) member in the first bay are assumed to have 70% and 30% reductions in Young's modulus, respectively, and all the other members are assumed to be undamaged. The first two vibration modes, corresponding to the bending of the frame along the x and y directions, respectively, are used to detect damage. The translational degrees of freedom of the 16 nodes, denoted by "S" in FIG. 10, along the x and y directions are assumed to be measured with 10% measurement noise. All the other degrees of freedom are estimated using the eigenvector expansion method discussed above and the measured modes are mass-normalized. The Young's moduli of all the members of the damaged truss are identified as shown in FIG. 10, with the maximum estimation error less than 7%. Note that the truss has closely spaced vibration modes. With the modes arranged in the order of increasing frequencies in each iteration, the method has effectively handled mode switching that has occurred in the damage detection process.

[0179] In summary, the damage detection method identifies stiffness parameters in structures, which have a small, medium, and large level of damage if the maximum reduction in the stiffnesses is within 30%, between 30 and 70%, and over 70%, respectively. A large level of damage is studied in many examples because this poses the most challenging case, with sever mismatch between the eigenparameters of the damaged and undamaged structures.

[0180] The damage detection method as embodied and broadly described herein can be applied to structures that can be modeled with beam elements. A beam element is an element that has one dimension that is much longer than the other two. This element is very good at modeling "I"-beams, rectangular beams, circular beams, "L"-angles, "C"-channels, pipes, and beams with varying cross sections. Structures that can be modeled with this element include, but are not limited to, lightning masts, light poles, traffic control poles, pillar type supports, bridges, pipelines, steel building frameworks, television, radio, and cellular towers, space structures, cranes, pipelines, railway tracks, and vehicle frames. Structures that can be modeled as beam elements are used simply for ease of discussion, and it is well understood that the damage detection method discussed above may be applied to structures that can be modeled by other elements using the finite element method or modeled by using other methods.

[0181] Damage Detection Using Changes of Natural Frequencies: Simulation and Experimental Validation

[0182] For structures such as beams and lightning masts in electric substations, using only the changes in the natural frequencies can relatively accurately detect the location(s) and extent of damage, even though the system equations are severely underdetermined in each iteration. This is an interesting finding as it is much easier to measure the natural frequencies than the mode shapes, and demonstrates the effectiveness of the iterative algorithm. Extensive numerical simulations on beams and lightning masts confirmed this finding. Experiments on the beam test specimens with different damage scenarios and a lightning mast in an electric substation validated the simulation results. The beam test specimens and the lightning mast are used as examples for demonstration purposes, and the method can be applied to other structures. Note that unlike the beam example shown earlier, where the Euler-Bernoulli beam finite element model is used, the Timoshenko beam finite element model is used in all the examples here. The Timoshenko beam theory is found to be more accurate in predicting the natural frequencies of the lightning masts and circular beams than the Euler-Bernoulli beam theory.

[0183] For a cantilever beam, simulation results show that the damage located at a position within 0-35% and 50-95% of the length of the beam from the cantilevered end can be easily detected with less than 5 measured natural frequencies, and the damage located at a position within 35-50% of the length of the beam from the cantilevered end and at a position within 5% of the length of the beam from the free end can be relatively accurately detected with 10-15 measured natural frequencies.

[0184] Numerical and Experimental Verification

[0185] Cantilever Aluminum Beams

[0186] Experimental damage detection results for four different scenarios are shown first, followed by various simulation results.

[0187] Scenario 1: Evenly-Distributed Damage Machined from the Top and the Bottom Surfaces of the Beam Test Specimen.

[0188] The aluminum beam test specimen shown in FIG. 12 is 45 cm long by 2.54 cm wide by 0.635 cm thick. It is divided into 40 elements (each element has a length of 1.125 cm). The beam has a section (from approximately 10 cm to 15 cm from the cantilevered end) of 5 cm long and 7.62E-4 m thick machined both from the top and the bottom surfaces of the beam. This corresponds to 56% of damage (or reduction of bending stiffness EI) along the length of five elements (from the 9th to the 13th element). Using the changes of the first 2 to 5 measured natural frequencies, damage is detected within 7 elements using 2 or 5 measured frequencies (from the 7th to the 13th element with 5 measured frequencies and from the 5th to the 11th element with 2 measured frequencies) and within 8 elements using 3 or 4 measured natural frequencies (both from the 6th to the 13th element), as shown in FIG. 13. With 5 measured frequencies the average damage of the 7 elements in FIG. 13, from 6.75 cm to 14.625 cm, is 46%. Note that the elements with damage less than 10% are not accounted for here. The extent of damage detected is slightly lower than the actual extent because the predicted damage occurs at 2 more elements (the 7th and 8th elements) than the actual one. The error results from the solution of the severely underdetermined system equations (5 equations with 80 unknowns).

[0189] Scenario 2: The Same Aluminum Beam Test Specimen as in Scenario 1 Clamped at the Other End.

[0190] The same beam was tested in the clamped-free configuration with the clamped end reversed, which placed the damage from 25 cm to 30 cm (from the 23rd to the 27th element) from the cantilevered end. The damage detection results with 3 to 5 measured frequencies are shown in FIG. 14. With 5 measured frequencies the average damage between 23.625 cm to 32.625 cm (from the 22nd to the 29th element) is 40%. Again the elements with damage less than 10% are not included.

[0191] Scenario 3: Undamaged Cantilever Aluminum Beam Test Specimen with the Same Dimensions as Above.

[0192] An undamaged aluminum beam test specimen was clamped at one end with the same configuration as shown in FIG. 12. With the first 3 to 4 measured frequencies the maximum error for the estimated bending stiffnesses of all the elements is within 10%, as shown in FIG. 15.

[0193] Scenario 4: A Cut of Small Width on a Cantilever Aluminum Beam Test Specimen, Shown in FIG. 16 with the Same Dimensions as Above.

[0194] The beam shown below has a cut that is 0.4191 cm deep and 0.1016 cm wide, which corresponds to a 96% reduction in bending stiffness at the cut. The beam is divided into 45 elements and the cut is located in the middle of the 23rd element. With 3 to 5 measured natural frequencies, the damage is detected at several elements surrounding the 23rd

element, as shown in FIG. 17. It was found there was a roughly 50%, 40%, and 60% reduction in stiffness at the 22nd, 23rd, and 24th element, respectively. The estimated damage extent at the above elements is lower than that at the cut because the damage is distributed along these elements.

[0195] To examine the effectiveness and robustness of the damage detection algorithm, various simulations with different damage scenarios were carried out. In this way, we can gain more insight concerning the accuracy of the finite element model, convergence of the estimated bending stiffnesses of all the elements of the beam with the increased numbers of measured natural frequencies and/or mode shapes, and region of the beam within which the damage can be detected with few measured frequencies. With the cantilever aluminum beam divided into 40 elements, the following two simulations have the similar damage location and extent to those in Scenarios 1 and 2 in the experiments:

[0196] Simulation 1: Uniform Damage Between 9.0 cm and 15.75 cm from the Cantilevered End of the Beam with the Same Dimensions as Discussed Above.

[0197] Simulation 2: Uniform Damage Between 29.25 cm and 36 cm from the Cantilevered End of the Beam with the Same Dimensions as Discussed Above.

[0198] Simulation results in FIG. 18 and FIG. 19 show that the damage can be relatively accurately detected with the first 3 to 5 measured frequencies, and can be accurately detected with the first 10 measured frequencies.

[0199] With the cantilever aluminum beam divided into the same number of elements, two more simulations are presented here: one for a multiple damage scenario—70% of damage at the 3rd element and 30% of damage at the 20th element, and the other for a 50% of uniform damage from the 16th to the 18th element (i.e., the damage is located at a position within 35-50% of the length of the beam from the cantilevered end).

[0200] Simulation 3: Multiple Damage of the Beam with the Same Dimensions as Discussed Above: 70% of Damage at the 3rd Element and 30% of Damage at the 20th Element.

[0201] Simulation results in FIG. 20 show that the multiple damage can be relatively accurately detected with the first 3 to 5 measured frequencies, and accurately detected with the first 10 measured frequencies.

[0202] Simulation 4: Uniform Damage from the 16th to the 18th Element of the Beam with the Same Dimensions as Discussed Above.

[0203] Simulation results in FIG. 21 show that the damage within 35-50% of the length of the beam from the cantilever end can be accurately detected with 10-15 measured frequencies.

[0204] Lightning Masts

[0205] The lighting mast shown in FIG. 22 has two sections of constant cross-sections and an eccentric spike. The lengths of the lower and upper sections are 6.89 m and 6.83 m, respectively, and that of the spike above the upper section is 1.4375 m. Both mode shapes and natural frequencies were measured for this mast. The mode shapes were measured by using a laser Doppler vibrometer. The natural frequencies were measured using both the laser Doppler vibrometer and an accelerometer. It takes about 0.5-1.5 days

to measure the mode shapes and about 30 minutes to measure the natural frequencies. It would be even more difficult to measure the mode shapes for some of the taller lightning masts, which are 100 and 130 feet tall. A finite element model was made using OpenFEM. Once the model was completed the measured and calculated natural frequencies and mode shapes were compared. The mast was expected to be undamaged, since by inspection the measured and calculated natural frequencies matched (Table 2). It was found that the first mode shape measurement is affected by wind and high modes are less affected by the wind. The measured frequencies are not affected by the wind and can be used for damage detection.

TABLE 2

Comparison of measured and calculated (from the finite element model) natural frequencies			
Mode #	Measured	FEM	Error %
1	1.17	1.18	-0.8648
2	5.10	5.23	-2.4304
3	7.83	7.89	-0.8418
4	8.17	8.67	-6.1104
5	16.60	16.55	0.31327
6	29.26	30.36	-3.7885
7	45.32	47.85	-5.5831
8	47.75	50.87	-6.5191
9	54.10	55.81	-3.1439
10	67.45	68.83	-2.0476
11	74.70	78.99	-5.7456

[0206] Damage detection was then performed using only the first 4 to 7 measured natural frequencies, as shown in Table 2. The mast is modeled by 40 elements; the lower section has 18 elements, the upper section has 15 elements, and the spike has 7 elements. The experimental damage detection results are shown in FIG. 23. The mast is modeled by 40 elements with 20 elements in each of the two sections. It appears that the elements around the joints near the middle of the mast (8.2 m in FIG. 23) and at the free end of the mast (13.72 m in FIG. 23) had some damage. This is most likely due to the fact that the joints were modeled in the finite element model as being infinitely stiff, which is almost never the case. Also, the spike is actually connected to the free end of the mast at two points. In the finite element model here it is assumed that the spike is attached to the mast along the whole line of contact that has a length of 0.34 m, which makes the model a little stiffer. Similar damage detection results were obtained with different numbers of measured frequencies.

[0207] Simulations for the same lightning mast as shown in FIG. 22 with different damage scenarios are carried out. Shown in FIG. 24 are the simulation results for the mast with 70% damage between 0.76 m and 1.15 m from the ground. Shown in FIG. 25 are the simulation results for the mast with 50% damage between 6.89 m and 7.35 m from the ground. In both cases the location and extent of damage can be relatively accurately detected using the first 5 measured natural frequencies and accurately detected using the first 8 or 10 measured frequencies.

[0208] Methods to Handle Some Ill-Conditioned System Equations

[0209] When the first order perturbation approach is used, one needs to solve in each iteration a system of linear algebraic equations

$$A\delta G = F \quad (47)$$

[0210] which are the linearized equations of (5) and (6), where A is the system matrix, F is the vector representing the differences between the measured and estimated natural frequencies and/or mode shapes, δG is the optimal changes in the stiffness parameters to be found. While the gradient and quasi-Newton methods can be used, the generalized inverse method is most efficient because it does not involve nested iterations, and thus $\delta G = A^+ F$, where A^+ is the generalized inverse of A . The problem (47) may be ill posed for certain cases, especially in the first several iterations, because A^+ can be relatively large and small changes in F can result in large changes in the solution δG . Since the stiffness parameters cannot be negative or greater than the corresponding values of the undamaged structure, the solution may not converge.

[0211] Ill-conditioning problems do not occur in all the examples described above. Sometimes they can occur. Consider, for example, a cantilever aluminum beam of the same dimensions as those of the beam shown in FIG. 12. The beam is divided into 36 elements and assumed to have 30% of damage at the 5th element and 90% of damage at the 18th element. The translational degrees of freedom of the first or second mode shape vector are used to detect damage. The system equations are determinate, and the ill-conditioning problem occurs in the iterations. When a natural frequency is also used in addition to an incomplete eigenvector described above, the ill-conditioning problem can also occur. The following regularization methods can be used to handle the ill-conditioning problem:

[0212] Method 1. Estimate A^+ from $(A^T A + \eta I)^{-1} A^T$, where η is a small positive constant that can be searched in several ways. One way is set $\eta = \mu \times 1.618 \times \min(10, \|\delta G\|_\infty)$, where $\mu \mu_\infty$ denotes the infinity norm, with the initial value $\eta = \|A^T A\|_\infty$, until $\|\delta G\|_\infty$ is less than 0.8, for example.

[0213] Method 2. To constrain the magnitude of δG , we include it in the objective function to be minimized. For example, we can minimize the following objective function

$$f(\delta G) = \sum_{j=1}^{N_s} \sum_{i=1}^{N_m} (F_i - A_{ij} \delta G_j)^2 + \sum_{j=1}^{N_m} (\delta G_j)^2 \quad (48)$$

[0214] instead of (35), where $N_m = n_3 + n_4 N_{nm}$ is the number of equations in (5) and (6). The optimal solution can be obtained by using the generalized inverse method for the expanded system $A^+ = [A; I]$ and the expanded vector $F^+ = [F; 0]$, where I is the $m \times m$ identity matrix and 0 is the $m \times 1$ zero vector.

[0215] Note that the solutions from the regularization methods are not strictly the optimal solutions for the original objective function in (35). With accurate and sufficient

measurement information and proper handling of the ill-conditioning problem, the system equations can become well conditioned in the last few iterations and regularization does not need to be applied. Consequently the stiffness parameters can be more accurately determined. Sometimes regularization may over constrain the magnitude of δG , and the termination criterion $\|\delta G\|_\infty < \epsilon$ may be satisfied during the regulation process. In this case, we may set

$$\delta G_i = \frac{3\epsilon \delta G_i}{\|\delta G\|_\infty}$$

[0216] to amplify the magnitude of δG , and the iteration is terminated after the system equations become well conditioned. Since the second regulation method does not need to search for η , it can be more effective when it works. When one carries out the damage detection procedures using different combinations of measured frequencies and mode shapes and obtains the same or similar stiffness parameters, one can have sufficient confidence on the results obtained.

[0217] Using only the translational degrees of freedom of the first eigenvector and the first regulation method, the estimated bending stiffnesses of all the elements of the beam are shown in FIG. 26A. Using the translational degrees of freedom of the second eigenvector and the first regulation method, the estimated bending stiffnesses of all the elements of the beam are shown in FIG. 26B. In both cases the locations of damage are exactly detected and the extent is relatively accurately determined. Using the translational degrees of freedom of the first eigenvector along with the first natural frequency and the first regulation method, the bending stiffnesses of all the elements of the beam are exactly determined, as shown in FIG. 26C.

[0218] Similarly, using the translational degrees of freedom of the first eigenvector and the second regulation method, the estimated bending stiffnesses of all the elements of the beam are shown in FIG. 27A. Using the translational degrees of freedom of the second eigenvector and the second regulation method, the estimated bending stiffnesses of all the elements of the beam are shown in FIG. 27B. In both cases the locations of damage are exactly detected and the extent is relatively accurately determined. Using the translational degrees of freedom of the first eigenvector along with the first natural frequency and the second regulation method, the bending stiffnesses of all the elements of the beam are exactly determined, as shown in FIG. 27C.

[0219] Conclusions

[0220] Thus, the sensitivities of eigenparameters of all orders may, for the first time, be derived using a multiple-parameter, general-order perturbation method. The higher-order solutions may be used to estimate the changes in the eigenparameters with large changes in the stiffness parameters. The perturbation method may be combined with an optimization method to form a robust iterative damage detection algorithm. The gradient and quasi-Newton methods can be used for the first or higher order system equations, and the generalized inverse method can be used efficiently with the first order system equations because it does not involve nested iterations. Including the higher-order perturbations can significantly reduce the number of

iterations when there is a large level of damage. A modified eigenvector expansion method is used to estimate the unmeasured component of the measured mode shape. For many cases, the location(s) and extent of damage can be relatively accurately detected using only measured natural frequencies. Methods to handle ill-conditioned system equations that may occasionally arise are developed and shown to be effective. Numerical simulations on different structures including spring-mass systems, beams, lightning masts, and frames show that with a small number of measured eigenparameters, the stiffness parameters of the damaged system may be accurately identified in all the cases considered. Experiments on the different beam test specimens and the lightning mast in an electric substation validated the theoretical predictions. The methodology can be readily applied to various operation structures of different sizes by incorporating their finite element models or other mathematical models.

[0221] One example of a practical application of this damage detection method is shown in FIG. 28, in which a structure 10 may represent any type of structure that can be modeled by beam elements, on which periodic damage assessment must be conducted. This includes, but is not limited to, structures such as lightning masts, utility poles, cell towers, and other such structures. A structure that can be modeled by beam elements is used simply for ease of discussion, and it is well understood that the general order perturbation method discussed above may be applied to a number of different structural members without departing from the spirit of the invention as embodied and broadly described herein.

[0222] The structure 10 divided into elements E_1 through E_n , and with nodes N_1 through N_n , is equipped with a sensor 40, such as, for example, an accelerometer. The sensor 40 is configured to measure a response to an impact F or a force from a shaker applied to the structure 10. The impact F may be applied in the form of a single impact, as shown in FIG. 28, or it may be in the form of a series of random impacts F_1 through F_n , as shown in FIG. 29. The location on the beam where the impact F is applied may be varied, but the impact F is preferably not applied at one of the nodal points of vibration modes whose natural frequencies and mode shapes need to be measured. In either instance, the sensor 40 senses a response in the structure 10 to the impact F or the force from the shaker, and transmits that response to a processor 20 equipped with, among other elements, the damage detection method 30 discussed above.

[0223] In accordance with the method as described above, upon receipt of the response signal from the sensor 40, the processor 20 accesses and performs the method 30 as previously discussed, and, as the data converges, determines an extent and location, by element, of any structural damage present in the structure 10.

[0224] Although the convergence of the system to resolution is not dependent on where the impact F is applied to the structure 10, a signal to noise ratio of the response may be increased, and an efficiency of the system optimized, as the application point of the impact F is moved away from a fixed point N_0 , if one needs to measure the natural frequencies and/or mode shapes of lower modes. Similarly, although the system will converge regardless of the average energy and timing of the impact F or series of impacts F_1 - F_n applied

to the structure 10, a signal to noise ratio of the response may be increased, and an efficiency of the system optimized based on a random series of impacts or the random shaker excitation to the structure 10, if the structure is large or slightly nonlinear or if there is an ambient excitation to the structure such as wind.

[0225] The structure 10 may be excited in a number of different manners. For example, an impact F may be applied manually or a shaker may be used, at any given point on the structure 10, excluding the fixed point N_0 , or the nodal points of vibration modes whose natural frequencies and/or mode shapes need to be measured. However, in an effort to increase the signal to noise ratio in the signal provided by the sensor 40 to the processor 30 if the structure is large or slightly nonlinear or if there is an ambient excitation to the structure such as wind and to provide the convenience and portability over the shaker test, a series of random impacts F_1 - F_n shown in FIG. 29 may be applied manually or by a specially designed device to generate the impact F . Although accurate and reliable damage assessments can be achieved regardless of how the impact F is applied to the structure 10, results may be improved using a random series impact method, which involves using a series of impacts F of random amplitudes and random arrival times. A series of random impacts has been shown to increase an energy input to the structure 10, improve the signal to noise ratio, especially in such situations as strong wind excitation, and average out slight nonlinearities that arise, for example, from bolted joints and extract linearized eigenparameters.

[0226] FIG. 29 illustrates a structure 10, sensor 40 and processor 20 similar to those shown in FIG. 28. An impact F in FIG. 29 is applied to the structure 10, at a location other than N_0 or one of the nodal points of vibration modes whose natural frequencies and/or mode shapes need to be measured, as a series of random impacts F_1 through F_n delivered at random amplitude and arrival time. These random impacts F_1 - F_n may be delivered manually, or, as shown in FIG. 30, may be delivered in an automated fashion through the use of a random impact hammer device 1550.

[0227] Different methods have been employed in conventional vibration testing in order to excite a test specimen. Shaker testing, in which a specimen is, simplistically, shaken in order to impart a high level of energy, can produce a high signal to noise ratio, and can induce random excitation, which can average out slight nonlinearities and extract linearized eigenparameter parameters. However, shaker testing is not practically employed in the field on relatively large structures, and can be cost prohibitive to conduct. Single impact hammer testing addresses the shortfalls of shaker testing, in that it is portable and inexpensive to conduct. However, single impact hammer testing falls short where shaker testing is strong, in that low energy input of single impact hammer testing produces a low energy input, a low signal to noise ratio with no randomization. To address the need for a system which combines the advantages of shaker testing and single impact hammer testing, a Random Impact Series method for hammer testing is presented which yields a high energy, high signal to noise ratio, random system. A novel stochastic model is developed to simulate the random impact series produced manually and to generate a random impact series for a specially designed random impact device.

[0228] FIG. 31 shows a random impact device 1550, according to one embodiment of the invention. Random

impact device 1550 includes random signal generating unit 1560 and a random impact actuator 1570 with impact applicator 1580. The impact applicator 1580 preferably includes a sensor 1581, such as a force transducer, attached at its tip. Sensor 1581 is preferably configured to send data to the spectrum analyzer in stiffness parameter unit 103 in order to obtain mode shape information, as discussed above in connection with FIG. 1A. Sensor 1581 can be coupled to the spectrum analyzer in any manner known in the art including, but not limited to, wire, optical fiber or even a wireless connection. Random impact signal generating unit 1560 generates outputs 1590 and 1591 to random impact actuator 1570. It should be appreciated that outputs 1590 and 1591 could be coupled to the random impact actuator 1570 in any manner known in the art including, but not limited to, cables, wires, optical fibers, wireless communications, and so forth.

[0229] Output 1590 corresponds to the amplitude ψ_p , as discussed below. In particular, random signal generating unit 1560 outputs a value corresponding to ψ_p , as discussed below. Output 1591 corresponds to τ_i , as discussed below.

[0230] Impact applicator 1580 is shown, for purposes of illustration, as impacting structure 1600 in a reciprocating motion. Impact applicator 1580 is shown to have an impact path 1610, such that when a structure 1600 lies within the impact region 1610, impact applicator 1580 impacts structure 1600 with a force of random amplitude that arrives at a random time, as discussed below. The impact applicator 1580 and impact region 1610 as shown in FIG. 31 is one possible embodiment, and other shapes and impact regions may be used while still falling within the scope of the present invention.

[0231] Although random signal generating unit 1560 is shown to output two outputs 1590 and 1591 that correspond to ψ_i and τ_i below, it should be understood that signal generating unit 1560 could output any signal or signals that ultimately results in random impact actuator 1570 driving impact applicator 1580 to impact structure 1600 with random arrival times τ_i and random amplitudes ψ_i .

[0232] As discussed above, vibration information is obtained by sensor 110, and is sent to stiffness parameter unit 103 via sensor coupler 113. The stiffness parameter unit 103 sends stiffness parameters to the damage information processor 123. While the random impact device can be used for damage detection purposes as discussed above, it can certainly be used just for obtaining the natural frequencies and/or mode shapes of the structure for modal testing purposes.

[0233] Experiments conducted on lightning masts by the applicant confirm that multiple impact testing performs better than single impact testing when there is wind excitation to the masts. Results are shown for a 65 foot tall mast with a 5 foot spike, as shown in FIG. 32, referred to hereinafter simply as a seventy foot tall mast. The mast has two constant cross section schedule 40 pipes of equal length. It can be seen from the results shown in FIGS. 33A-33B that the multiple impact test has much better coherence, is less noisy away from the resonances, and can pick up the modes that were missing in the single impact test. The multiple impact test is better at exciting the lower modes that can also be excited by the wind, which can be seen by comparing the frequency response functions (FRF) between 0 and 30 Hz.

It can be seen from the FRF for the multiple impact tests that there are some modes that are missed at near 4 Hz and 7 Hz with the single impact test, and the mode at 10 Hz is much improved compared to the single impact test.

[0234] A stochastic model will now be discussed which describes the random impact series F_1-F_n , modeled as a Poisson process. The Poisson process is one of a general class of processes that arise in problems concerning the counting of events in the course of time. The force pulses in the series are assumed to have an arbitrary, deterministic shape function and random amplitudes and arrival times. The force signal in a finite time interval is shown to consist of wide sense stationary and non-stationary parts. The expectations of the average power densities associated with the entire force signal and the stationary part of the signal are derived and compared, and the power spectral density is related to the average power density and the autocorrelation function associated with the stationary part of the force signal. Numerical simulation is conducted to validate analytical predictions, and a relationship between the Fourier transform and the discrete Fourier transform used in a numerical simulation is produced. Experiments on the four bay space frame, as shown in FIG. 10, validated the distributions of the random variables and the Poisson process.

[0235] Stochastic Model of a Random Impact Series

[0236] A random impact series is modeled here as a sum of force pulses with the same shape and random amplitudes and arrival times:

$$x(t) = \sum_{i=1}^{N(t)} \psi_i y(t - \tau_i) \quad t \in (0, \infty) \quad (49)$$

[0237] where t is time, $x(t)$ is the time function of the force signal, $\tau_i \in (0, t]$ is the random arrival time of the i -th pulse, and $y(t-\tau_i)$ is the deterministic shape function for all the pulses, ψ_i is the random variable describing the amplitude of the i -th pulse, and $N(t)$ is the number of the pulses that have arrived during the time interval $(0, t]$ and is modeled as a Poisson process with stationary increments. All the pulses are assumed to be of width $\Delta\tau$, and $y(t-\tau_i)$ satisfies $y(t-\tau_i)=0$ if $t-\tau_i < 0$ and $t-\tau_i > \tau_i + \Delta\tau$.

[0238] Since a finite time record is used for the force signal in modal testing, we consider only the pulses that arrive during the time interval $(0, T]$ of length T , as shown in FIG. 34. Note that $y(0)$ and $y(\Delta\tau)$ do not have to be equal to zero in this model. Because the pulses arriving after time t ($t < T$) will not affect the force signal at time t , the random process $N(t)$ in (49) can be replaced by $N(T)$. Also, if a pulse arrives at time T , it will vanish at time $T + \Delta\tau$. The last pulse in FIG. 34 arrives at time $T_{N(T)}$ and ends at a time between T and $T + \Delta\tau$. To include completely this last possible pulse, we consider the time interval $t \in (0, T + \Delta\tau]$. Equation (49) is rewritten as

$$x(t) = \sum_{i=1}^{N(T)} \psi_i y(t - \tau_i), \quad \tau_i \in (0, T] \text{ and } t \in (0, T + \Delta\tau) \quad (50)$$

[0239] For the Poisson process $N(t)$ with stationary increments, the probability of the event $\{N(t)=n\}$, where n is an integer, is

$$P_{N(t)}(n, t) = \frac{e^{-\lambda t} (\lambda t)^n}{n!},$$

[0240] where λ is the constant arrival rate of the pulses. By replacing t with T , the probability of the event $\{N(T)=n\}$ is

$$P_{N(T)}(n, T) = \frac{e^{-\lambda T} (\lambda T)^n}{n!} \quad (51)$$

[0241] All the arrival times τ_i , where $i=1,2,3, \dots, N(T)$, are identically distributed, mutually independent random variables. Because the arrival rate of the pulses is constant, the arrival times τ_i are uniformly distributed in $[0, T]$ with the probability density function

$$P_{\tau_i}(\tau) = \begin{cases} \frac{1}{T}, & 0 \leq \tau \leq T \\ 0, & \text{elsewhere} \end{cases} \quad (52)$$

[0242] Similarly, ψ_i ($i=1,2, \dots, N(T)$) are identically distributed random variables, which are mutually independent and independent of the distribution of the arrival times τ_i . While the distribution of ψ_i ($i=1,2, \dots, N(T)$) is not used in the subsequent derivation, it is assumed that ψ_i satisfy the Gaussian distribution with the probability density function

$$p_{\psi_i}(\psi) = \frac{1}{\sqrt{2\pi} \sigma} e^{-\frac{(\psi-\mu)^2}{2\sigma^2}}, \quad 0 < \psi < \infty \quad (53)$$

[0243] where $\mu=E[\psi_i]$ is the mean and $\sigma^2=E[\psi_i^2]-E^2[\psi_i]$ is the variance of ψ_i . While the distribution in (53) is not used in the analytical derivations, it is used in the numerical simulation and validated experimentally for a manually applied random impacts on a four bay space frame, as shown in FIG. 10.

[0244] Force Spectrum and its Expectation

[0245] The force spectrum is the Fourier transform of the force signal in (50):

$$X(j\omega) = F[x(t)] = \quad (54)$$

-continued

$$= \int_{-\infty}^{\infty} \left\{ \sum_{i=1}^{N(T)} \psi_i y(t - \tau_i) \right\} e^{-j\omega t} dt = \sum_{i=1}^{N(T)} \psi_i \int_{\tau_i}^{\tau_i + \Delta\tau} y(t - \tau_i) e^{-j\omega t} dt$$

[0246] where F denotes Fourier transform, $X(j\omega)$ is the Fourier transform of $x(t)$, ω is the angular frequency, and $j = \sqrt{-1}$. Let $u=t-\tau_i$, then $t=u+\tau_i$ and $dt=du$. Equation (54) becomes

$$X(j\omega) = \sum_{i=1}^{N(T)} \psi_i e^{-j\omega\tau_i} \int_0^{\Delta\tau} y(u) e^{-j\omega u} du \quad (55)$$

[0247] Since the integral in (55) is a deterministic function, the expectation of the force spectrum is

$$E[X(j\omega)] = E \left[\sum_{i=1}^{N(T)} \psi_i e^{-j\omega\tau_i} \right] \int_0^{\Delta\tau} y(u) e^{-j\omega u} du \quad (56)$$

[0248] Using the expression for conditional expectations, $E[E[V|U]]=E(V)$, where $U=N(T)$ and

$$V = \sum_{i=1}^{N(T)} \psi_i e^{-j\omega\tau_i},$$

[0249] we have from (56)

$$\begin{aligned} E[X(j\omega)] &= E \left[E \left[\sum_{i=1}^{N(T)} \psi_i e^{-j\omega\tau_i} \right] \middle| N(T) \right] \int_0^{\Delta\tau} y(u) e^{-j\omega u} du \\ &= \sum_{n=0}^{\infty} P_{N(T)}(n, T) E \left[\sum_{i=1}^{N(T)} \psi_i e^{-j\omega\tau_i} \right] \int_0^{\Delta\tau} y(u) e^{-j\omega u} du \end{aligned} \quad (57)$$

[0250] Since $\psi_i e^{-j\omega\tau_i}$ ($i=1,2, \dots, n$) are independent of each other and ψ_i is independent of $e^{-j\omega\tau_i}$, we have

$$E \left[\sum_{i=1}^n \psi_i e^{-j\omega\tau_i} \right] = \sum_{i=1}^n E[\psi_i e^{-j\omega\tau_i}] = \sum_{i=1}^n E[\psi_i] E[e^{-j\omega\tau_i}] \quad (58)$$

[0251] Since ψ_i ($i=1,2, \dots, n$) are identically distributed random variables and so are τ_i ($i=1,2, \dots, n$), we have from (58)

$$E \left[\sum_{i=1}^n \psi_i e^{-j\omega\tau_i} \right] = n E[\psi_1] E[e^{-j\omega\tau_1}] \quad (59)$$

[0252] Substituting (59) into (57) yields

$$E[X(j\omega)] = \sum_{n=0}^{\infty} P_{|v|}(n, T) n E[\psi_1] \left[\int_{-\infty}^{\infty} e^{-j\omega\tau} p_{\tau_1}(\tau) d\tau \right] \int_0^{\Delta T} y(u) e^{-j\omega u} du \quad (60)$$

[0253] Substituting (51) and (52) into (60) yields

$$\begin{aligned} E[X(j\omega)] &= \sum_{n=0}^{\infty} \left[\frac{(\lambda T)^n e^{-\lambda T}}{n!} \right] n E[\psi_1] \left[\int_0^T \left(\frac{1}{T} \right) e^{-j\omega\tau} d\tau \right] \\ &\quad \int_0^{\Delta T} y(u) e^{-j\omega u} du \\ &= \sum_{n=1}^{\infty} \frac{(\lambda T)^{n-1} e^{-\lambda T}}{(n-1)!} (\lambda T) E[\psi_1] \left\{ \frac{e^{-j\omega T} - 1}{-j\omega T} \right\} \\ &\quad \int_0^{\Delta T} y(u) e^{-j\omega u} du \\ &= \frac{\lambda E[\psi_1] (1 - e^{-j\omega T})}{j\omega} \int_0^{\Delta T} y(u) e^{-j\omega u} du \end{aligned} \quad (61)$$

[0254] where Taylor expansion of $e^{\lambda T}$ has been used.

[0255] Average Power Density of $x(t)$ in $[0, T + \Delta T]$ and its Expectation

[0256] The average power density of the force signal in (50) is defined as

$$S_1(\omega) = \frac{X(j\omega) X^*(j\omega)}{T + \Delta T} \quad (62)$$

[0257] where $X^*(j\omega)$ is the complex conjugate of $X(j\omega)$:

$$X^*(j\omega) = \sum_{n=1}^{N(T)} \psi_1 e^{j\omega\tau_1} \int_0^{\Delta T} y(u) e^{j\omega u} du \quad (63)$$

[0258] Substituting (55) and (53) into (62) yields

$$\begin{aligned} S_1(\omega) &= \frac{\sum_{m=1}^{N(T)} \psi_m e^{-j\omega\tau_m} \int_0^{\Delta T} y(u) e^{-j\omega u} du}{T + \Delta T} \\ &\quad \sum_{n=1}^{N(T)} \psi_n e^{j\omega\tau_n} \int_0^{\Delta T} y(v) e^{j\omega v} dv \\ &= \frac{\left(\int_0^{\Delta T} \int_0^{\Delta T} y(u) y(v) e^{-j\omega(u-v)} du dv \right)}{T + \Delta T} \\ &\quad \sum_{m=1}^{N(T)} \sum_{n=1}^{N(T)} \psi_m \psi_n e^{j\omega(\tau_n - \tau_m)} \end{aligned} \quad (64)$$

[0259] Let $k = u - v$, then $u = k + v$ and $du = dk$. The double integral in (64) becomes

$$\begin{aligned} \int_{-\Delta T}^{\Delta T} \int_0^{\Delta T} y(u) y(v) e^{-j\omega(u-v)} du dv &= \\ \int_0^{\Delta T} dv \int_{-v}^{\Delta T} y(v+k) y(v) e^{-j\omega k} dk &+ \\ \int_0^{\Delta T} dv \int_0^{-v+\Delta T} y(v+k) y(v) e^{-j\omega k} dk \end{aligned} \quad (65)$$

[0260] Interchanging the order of integration in (65) yields

$$\begin{aligned} \int_{-\Delta T}^{\Delta T} \int_0^{\Delta T} y(u) y(v) e^{-j\omega(u-v)} du dv &= \\ \int_{-\Delta T}^{\Delta T} dk \int_k^{\Delta T} y(v+k) y(v) e^{-j\omega k} dv &+ \\ \int_0^{\Delta T} dk \int_0^{-k+\Delta T} y(v+k) y(v) e^{-j\omega k} dv \end{aligned} \quad (66)$$

[0261] Let $v+k=y$, then $v=y-k$ and $dv=dy$. The first integral on the right-hand side of (66) becomes

$$\begin{aligned} \int_{-\Delta T}^{\Delta T} dk \int_k^{\Delta T} y(v+k) y(v) e^{-j\omega k} dv &= \\ \int_{-\Delta T}^{\Delta T} dk \int_0^{\Delta T-k} y(y) y(y-k) e^{-j\omega k} dy \end{aligned} \quad (67)$$

[0262] Changing y in (67) back to v and substituting the resulting expression into (66) yields

$$\begin{aligned} \int_{-\Delta T}^{\Delta T} \int_0^{\Delta T} y(u) y(v) e^{-j\omega(u-v)} du dv &= \\ \int_{-\Delta T}^{\Delta T} \int_0^{\Delta T-|k|} y(v+|k|) y(v) dv e^{-j\omega k} dk \end{aligned} \quad (68)$$

[0263] Noting that

$$\int_0^{\Delta T-|k|} y(v+|k|) y(v) dv$$

[0264] is an even function of k , we have

$$\begin{aligned} \int_0^{\Delta T-|k|} y(v+|k|) y(v) e^{-j\omega k} dk &= \\ \int_0^{\Delta T-|k|} y(v+|k|) y(v) \cos(\omega k) dk \end{aligned} \quad (69)$$

[0265] Substituting (69) into (68) and substituting the resulting expression into (64) yields

$$S_1(\omega) = \frac{1}{T + \Delta\tau} \left(\int_{-\Delta\tau}^{\Delta\tau} \int_0^{\Delta\tau - |t|} y(v + |t|) y(v) dv \cos \omega k dk \right) \quad (70)$$

$$\sum_{m=1}^{N(T)/2} \sum_{n=1}^{N(T)} \phi_{m,n} \psi_n e^{j\omega \Delta\tau (1 - \gamma_m)}$$

[0266] Since the double integral in (70) is deterministic, we have

$$E[S_1(\omega)] = \frac{1}{T + \Delta\tau} \left(\int_{-\Delta\tau}^{\Delta\tau} \int_0^{\Delta\tau - |t|} y(v + |t|) y(v) dv \cos \omega k dk \right) \quad (71)$$

$$E \left[\sum_{m=1}^{N(T)/2} \sum_{n=1}^{N(T)} \phi_{m,n} \psi_n e^{j\omega \Delta\tau (1 - \gamma_m)} \right]$$

[0267] Since

$$E \left\{ \sum_{m=1}^{N(T)/2} \sum_{n=1}^{N(T)} \phi_{m,n} \psi_n \sin[j\omega(\tau_l - \tau_m)] \right\} = 0, \psi_l(l = 1, 2, \dots, N(T))$$

[0268] are identically distributed random variables, and so are τ_l ($l=1, 2, \dots, N(T)$), we have

$$E \left[\sum_{m=1}^{N(T)/2} \sum_{n=1}^{N(T)} \phi_{m,n} \psi_n e^{j\omega \Delta\tau (1 - \gamma_m)} \right] = E \left[\sum_{m=1}^{N(T)/2} \sum_{n=1}^{N(T)} \phi_{m,n} \psi_n \cos \omega(\tau_l - \tau_m) \right] = \quad (72)$$

$$E \left[\sum_{n=1}^{N(T)} \psi_n^2 + \sum_{m=1}^{N(T)/2} \sum_{n=1}^{N(T)} \phi_{m,n} \psi_n \cos \omega(\tau_l - \tau_m) \right] E$$

$$\left[\sum_{m=1}^{N(T)/2} \sum_{n=1}^{N(T)} \phi_{m,n} \psi_n \cos \omega(\tau_l - \tau_m) \right]$$

$$\{N(T)\psi_1^2 + [N^2(T) - N(T)]\psi_1^2 \cos \omega(\tau_1 - \tau_2)\}$$

[0269] Since τ_1 and τ_2 are independently, uniformly distributed random variables in $[0, T]$, the probability density function of $\tau_1 - \tau_2$ is

$$p_{\tau_1 - \tau_2}(\tau) = \begin{cases} \frac{T - |\tau|}{T^2}, & -T \leq \tau \leq T \\ 0, & \text{elsewhere} \end{cases} \quad (73)$$

[0270] Using (51) and (73) in (72) yields

$$E \left[\sum_{m=1}^{N(T)/2} \sum_{n=1}^{N(T)} \phi_{m,n} \psi_n e^{j\omega \Delta\tau (1 - \gamma_m)} \right] = \sum_{n=0}^{\infty} P_{10}(n, T) n E[\psi_1^2] + \quad (74)$$

$$\sum_{n=0}^{\infty} P_{10}(n, T) (n^2 - n) E[\psi_1^2]$$

$$\text{-continued}$$

$$\int_{-\infty}^{\infty} \cos(\omega\tau) p_{\tau_1 - \tau_2}(\tau) d\tau$$

$$= \lambda T E[\psi_1^2] + 2\lambda^2 E^2[\psi_1] \frac{1 - \cos(\omega T)}{\omega^2}$$

[0271] Substituting (74) into (71) yields

$$E[S_1(\omega)] = \frac{1}{T + \Delta\tau} \left[\int_{-\Delta\tau}^{\Delta\tau} \int_0^{\Delta\tau - |t|} y(v + |t|) y(v) dv \cos \omega k dk \right] \times \quad (75)$$

$$\left\{ 2\lambda^2 E^2[\psi_1] \frac{1 - \cos(\omega T)}{\omega^2} + \lambda T E[\psi_1^2] \right\}$$

[0272] Mean and Autocorrelation Functions of $x(t)$

[0273] The first-order cumulant function of $x(t)$ in (50), $\kappa_1[x(t)]$, is equal to its mean function, $E[x(t)]$. The second-order cumulant function of $x(t)$, $\kappa_2[x(t_1), x(t_2)]$, is related to its autocorrelation function, $E[x(t_1)x(t_2)]$ through

$$E[x(t_1)x(t_2)] = \kappa_2[x(t_1), x(t_2)] + \kappa_1[x(t_1)]\kappa_1[x(t_2)] \quad (76)$$

[0274] where t_1 and t_2 are any two time instants in $[0, T + \Delta\tau]$. Following the derivations, the first- and second-order cumulant functions of $x(t)$ are

$$\kappa_1[x(t)] = E[x(t)] = \lambda E[\psi_1] \int_0^T y(t - \alpha) d\alpha \quad (77)$$

$$\kappa_2[x(t_1), x(t_2)] = \int_0^{\Delta\tau} \int_0^{\Delta\tau} \kappa_{2,\alpha\beta}(t_1, t_2) = \lambda E[\psi_1^2] \int_0^T \int_0^T y(t_1 - \alpha) y(t_2 - \beta) d\alpha d\beta \quad (78)$$

[0275] where $t \in [0, T + \Delta\tau]$. Let $t - \alpha = u$ in (75), then $d\alpha = -du$. We have from (77)

$$E[x(t)] = \lambda E[\psi_1] \int_{T-\tau}^T y(u) du \quad (79)$$

[0276] Let

$$W(t) = \int_0^T y(u) du \quad (80)$$

[0277] Noting that $y(u)=0$ when $u<0$ and $u>\Delta\tau$, we have from (79)

$$E[x(t)] = \begin{cases} \lambda E[\psi_1] W(t), & 0 < t < \Delta\tau \\ \lambda E[\psi_1] W(\Delta\tau), & \Delta\tau \leq t \leq T \\ \lambda E[\psi_1] [W(\Delta\tau) - W(t - T)], & T < t \leq T + \Delta\tau \end{cases} \quad (81)$$

[0278] where $T > \Delta\tau$ is assumed. Let $t_1 - \alpha = u$ and $t_2 - \beta = k$ in (78), then $d\alpha = -du$ and $t_2 - \alpha = u + k$. We have from (78)

$$\kappa_{2,\alpha\beta}(t_1, t_2) = \lambda E[\psi_1^2] \int_{t_1 - \tau}^T y(u) y(u + k) du \quad (82)$$

[0279] When $|k| > \Delta\tau$, $y(u)y(u+k)=0$ and hence $\kappa_{xx}(t_1, t_2)=0$. When $0 \leq k \leq \Delta\tau$, we have from (82) for different t_1

$$\kappa_{xx}(t_1, t_2) = \quad (83)$$

$$\begin{cases} \lambda E[\psi_1^2] \int_0^{t_1} y(u)y(u+k)du, & 0 \leq t_1 < \Delta\tau - k \\ \lambda E[\psi_1^2] \int_0^{\Delta\tau-k} y(u)y(u+k)du, & \Delta\tau - k \leq t_1 \leq T \\ \lambda E[\psi_1^2] \int_{t_1-T}^{\Delta\tau-k} y(u)y(u+k)du, & T < t_1 \leq T + \Delta\tau - k \\ 0, & T + \Delta\tau - k < t_1 \leq T + \Delta\tau \end{cases}$$

[0280] When $-\Delta\tau \leq k < 0$, we have from (82) for different t_1

$$\kappa_{xx}(t_1, t_2) = \begin{cases} \lambda E[\psi_1^2] \int_{-k}^{t_1} y(u)y(u+k)du, & -k \leq t_1 < \Delta\tau \\ \lambda E[\psi_1^2] \int_{-k}^{\Delta\tau} y(u)y(u+k)du, & \Delta\tau \leq t_1 \leq T - k \\ \lambda E[\psi_1^2] \int_{t_1-T}^{\Delta\tau} y(u)y(u+k)du, & T - k < t_1 \leq T + \Delta\tau \\ 0, & 0 \leq t_1 < -k \end{cases} \quad (84)$$

[0281] Let $u+k=v$ in (84), then $u=v-k$ and $du=dv$. We have from (84) after changing v back to u

$$\kappa_{xx}(t_1, t_2) = \begin{cases} \lambda E[\psi_1^2] \int_0^{t_1+k} y(u-k)y(u)du, & -k \leq t_1 < \Delta\tau \\ \lambda E[\psi_1^2] \int_0^{\Delta\tau+k} y(u-k)y(u)du, & \Delta\tau \leq t_1 \leq T - k \\ \lambda E[\psi_1^2] \int_{t_1-T-k}^{\Delta\tau+k} y(u-k)y(u)du, & T - k < t_1 \leq T + \Delta\tau \\ 0, & 0 \leq t_1 < -k \end{cases} \quad (85)$$

[0282] Combining the second equations in (83) and (85), we have for t_1 and t_2 in $[\Delta\tau, T]$

$$\kappa_{xx}(t_1, t_2) = \lambda E[\psi_1^2] \int_0^{\Delta\tau-|k|} y(u)y(u+|k|)du \quad (86)$$

[0283] Since by the second equation in Eq. (81), $E[x(t)]$ is a constant for $t \in [\Delta\tau, T]$, and by (86), $\kappa_{xx}(t_1, t_2)$ is a function of $k=t_2-t_1$ for t_1 and t_2 in $[\Delta\tau, T]$, $x(t)$ is a wide-sense stationary random process in $[\Delta\tau, T]$. Substituting the second equation in (81) and (86) into (76) yields the autocorrelation function for t_1 and t_2 in $[\Delta\tau, T]$

$$\begin{aligned} R_{xx}(\lambda) \triangleq E[x(t_1)x(t_2)] &= \\ \lambda E[\psi_1^2] \int_0^{\Delta\tau-|k|} y(u)y(u+|k|)du + \lambda^2 E^2[\psi_1] W^2(\Delta\tau) \end{aligned} \quad (87)$$

[0284] Fourier Transform of the Mean Function of $x(t)$ and its Equivalence to $E[X(\omega)]$

[0285] Applying the Fourier transform to $E[x(t)]$ in Eq. (81) yields

$$F[E[x(t)]] = \lambda E[\psi_1] \left\{ \int_0^{\Delta\tau} W(t)e^{-j\omega t} dt + \int_{\Delta\tau}^T W(\Delta\tau)e^{-j\omega \Delta\tau} dt + \int_T^{T+\Delta\tau} [W(\Delta\tau) - W(t-\tau)]e^{-j\omega t} dt \right\} \quad (88)$$

[0286] The three integrals in (88) are referred to as I_1, I_2 , and I_3 , respectively. Consider first the third integral in (88)

$$I_3 = \int_T^{T+\Delta\tau} [W(\Delta\tau) - W(t-T)]e^{-j\omega t} dt \quad (89)$$

[0287] Let $t-T=\theta$ in (88), then $t=T+\theta$ and $dt=d\theta$. We have from Eq. (89)

$$I_3 = e^{-j\omega(T+\Delta\tau)} \int_0^{\Delta\tau} W(\Delta\tau)e^{-j\omega\theta} d\theta - e^{-j\omega T} \int_0^{\Delta\tau} W(\theta)e^{-j\omega\theta} d\theta \quad (90)$$

[0288] Changing θ in (90) back to t and combining I_1 and I_3 yields

$$\frac{I_1 + I_3}{j\omega} = e^{-j\omega(T+\Delta\tau)} \int_0^{\Delta\tau} W(\Delta\tau)e^{-j\omega t} dt + (1 - e^{-j\omega T}) \int_0^{\Delta\tau} W(t)e^{-j\omega t} dt \quad (91)$$

[0289] Adding I_2 to (91), simplifying the expression, and substituting it into (88) yields

$$\begin{aligned} F[E[x(t)]] &= \\ \lambda E[\psi_1] \left\{ (1 - e^{-j\omega T}) \int_0^{\Delta\tau} W(t)e^{-j\omega t} dt + e^{-j\omega T} \int_0^{\Delta\tau} W(\Delta\tau) e^{-j\omega t} dt + \int_{\Delta\tau}^T W(\Delta\tau)e^{-j\omega t} dt \right\} &= \lambda E[\psi_1] \\ (1 - e^{-j\omega T}) W(\Delta\tau) \left[\frac{1}{j\omega} + \int_0^{\Delta\tau} \frac{W(t)}{W(\Delta\tau)} - 1 \right] e^{-j\omega T} dt \end{aligned} \quad (92)$$

[0290] We will show that $F[E[x(t)]]$ in (92) is equivalent to $E[X(\omega)]$ in (91). By (80), we have

$$W(t) = \begin{cases} 0, & t \in (-\infty, 0) \\ \int_0^t f(\tau) d\tau, & t \in [0, \Delta\tau] \\ W(\Delta\tau), & t \in (\Delta\tau, \infty) \end{cases} \quad (93)$$

[0291] The integral in (61) can be written as

$$\begin{aligned} \int_0^{\Delta\tau} y(u)e^{-j\omega u} du &= \int_0^{\Delta\tau} y(u)du + \int_0^{\Delta\tau} y(u)(e^{-j\omega u} - 1)du \\ &= \int_0^{\Delta\tau} y(u)du - j\omega \int_0^{\Delta\tau} y(u) \int_0^u e^{-j\omega \tau} d\tau du \end{aligned} \quad (94)$$

[0292] Interchanging the order of integration in the double integral in (94) and using (93) yields

$$\begin{aligned} \int_0^{\Delta\tau} y(u) e^{-\beta u} du &= \\ &= \int_0^{\Delta\tau} y(u) du - \int_0^{\Delta\tau} \int_0^{\Delta\tau} y(u) e^{-\beta v} dv du \\ &= W(\Delta\tau) \left\{ 1 + \int_0^{\Delta\tau} \left(\frac{W(v)}{W(\Delta\tau)} - 1 \right) e^{-\beta v} dv \right\} \end{aligned} \quad (95)$$

[0293] Substituting (95) into (61) yields (91). This shows that the expectation E and the Fourier transform F are commutative as both are linear operators.

[0294] Equation (92) consists of two parts: the first part,

$$\lambda E[\phi_1](1 - e^{-\beta \Delta\tau}) W(\Delta\tau) \frac{1}{\beta},$$

[0295] is the Fourier transform of the stationary part of $E[x(t)]$ in $[\Delta\tau, T]$, and the second part,

$$\lambda E[\phi_1](1 - e^{-\beta \Delta\tau}) W(\Delta\tau) \int_0^{\Delta\tau} \left(\frac{W(t)}{W(\Delta\tau)} - 1 \right) e^{-\beta t} dt,$$

[0296] is the sum of the Fourier transforms of the nonstationary parts of $E[x(t)]$ in $[0, \Delta\tau]$ and $[T, T + \Delta\tau]$. When $\Delta\tau \rightarrow 0$, since

$$\frac{W(t)}{W(\Delta\tau)} - 1$$

[0297] is finite,

$$\int_0^{\Delta\tau} \left(\frac{W(t)}{W(\Delta\tau)} - 1 \right) e^{-\beta t} dt,$$

[0298] and consequently the second part of $E[X(j\omega)]$, approaches zero.

[0299] Average Power Density of $x(t)$ in $[\Delta\tau, T]$, Its Expectation, and Power Spectral Density

[0300] Since $x(t)$ is stationary in $[\Delta\tau, T]$, the average power density of $x(t)$ in $[\Delta\tau, T]$ is defined as

$$S_2(\omega) = \frac{X_s(j\omega)X_s^*(j\omega)}{T - \Delta\tau} \quad (96)$$

[0301] where $X_s(j\omega) = \int_{\Delta\tau}^T x(t) e^{-j\omega t} dt$. Taking the expectation of (96) yields

$$E[S_2(\omega)] = \frac{1}{T - \Delta\tau} \int_{\Delta\tau}^T \int_{\Delta\tau}^T E[x(t_1)x(t_2)] e^{-\beta \omega t_1 - \beta \omega t_2} dt_1 dt_2 \quad (97)$$

[0302] Let $k = t_2 - t_1$ in (97), then $dk = dt_2$. Since $E[x(t_1)x(t_2)] = R_{xx}(k)$, (97) becomes after interchanging the order of integration

$$\begin{aligned} E[S_2(\omega)] &= \frac{1}{T - \Delta\tau} \int_{\Delta\tau}^T \int_{\Delta\tau}^{T-t_1} R_{xx}(k) e^{-\beta \omega k} dk dt_1 \\ &= \int_{-(T-\Delta\tau)}^{T-\Delta\tau} R_{xx}(k) \left(1 - \frac{|k|}{T - \Delta\tau} \right) e^{-\beta \omega k} dk \end{aligned} \quad (98)$$

[0303] Substituting (87) into (98) yields

$$\begin{aligned} E[S_2(\omega)] &= \lambda E[\phi_1^2] \\ &= \int_{-(T-\Delta\tau)}^{T-\Delta\tau} \int_0^{\Delta\tau - |k|} y(u + |k|) y(u) du \left(1 - \frac{|k|}{T - \Delta\tau} \right) e^{-\beta \omega k} dk + \\ &\quad 2\lambda^2 E^2[\phi_1] W^2(\Delta\tau) \int_{-(T-\Delta\tau)}^{T-\Delta\tau} \left(1 - \frac{|k|}{T - \Delta\tau} \right) e^{-\beta \omega k} dk \end{aligned} \quad (99)$$

[0304] Noting that $y(u)y(u + |k|) = 0$ when $|k| > \Delta\tau$ and

$$\int_0^{\Delta\tau - |k|} y(u + |k|) y(u) du \left(1 - \frac{|k|}{T - \Delta\tau} \right)$$

[0305] an even function of $|k|$, we have from (99)

$$\begin{aligned} E[S_2(\omega)] &= 2\lambda^2 E^2[\phi_1] W^2(\Delta\tau) \frac{1 - \cos \omega(T - \Delta\tau)}{\omega^2(T - \Delta\tau)} + \lambda E[\phi_1^2] \\ &\quad \int_{-\Delta\tau}^{\Delta\tau} \int_0^{\Delta\tau - |k|} y(u + |k|) y(u) du \left(1 - \frac{|k|}{T - \Delta\tau} \right) \cos \omega k dk \end{aligned} \quad (100)$$

[0306] where $T > 2\Delta\tau$ has been assumed.

[0307] The power spectral density of $x(t)$ can be obtained from (100) by increasing T to infinity

$$\begin{aligned} S_x(\omega) &= \lim_{T \rightarrow \infty} S_2(\omega) = 2\pi \lambda^2 E^2[\phi_1] W^2(\Delta\tau) \delta(\omega) + \\ &\quad \lambda E[\phi_1^2] \int_{-\Delta\tau}^{\Delta\tau} \int_0^{\Delta\tau - |k|} f(u + |k|) f(u) \cos(\omega k) dk \end{aligned} \quad (101)$$

[0308] where we have used

$$\lim_{T \rightarrow \infty} \frac{1 - \cos \omega(T - \Delta\tau)}{\pi \omega^2(T - \Delta\tau)} = \lim_{T \rightarrow \infty} \frac{2 \sin \frac{\omega(T - \Delta\tau)}{2}}{2\pi \omega^2(T - \Delta\tau)} = \delta(\omega) \quad (102)$$

[0309] in which $\delta(\omega)$ is the Dirac delta function. The power spectral density can also be obtained from (98) by increasing T to infinity

$$S_x(\omega) = \lim_{T \rightarrow \infty} E[S_x(\omega)] = \int_{-\infty}^{\infty} R_{xx}(k) e^{j\omega k} dk = \int_{-\infty}^{\infty} R_{xx}(k) \delta(\omega - \omega_k) d\omega_k \quad (103)$$

[0310] where $R_{xx}(-k) = R_{xx}(k)$ has been used. Equation (103) is the well-known Wiener-Khinchine theorem, which states the power spectral density is the Fourier transform of the autocorrelation function. Substituting (87) into (83), and noting that $I(u)I(u+k) \neq 0$ when $|k| > \Delta\tau$ and the Fourier transform of 1 is $2\pi\delta(\omega)$, yields (101). Note that the power spectral density is only defined for a wide-sense stationary process with an infinite time record. When the mean amplitude of each pulse $E[\psi_i]$ is not equal to zero, there is an associated delta function in the power spectral density.

[0311] Comparison of $E[S_1(\omega)]$ and $E[S_2(\omega)]$

[0312] By (100), $E[S_2(\omega)]$ consists of two parts: the first part,

$$2\lambda^2 E^2[\psi_i] W_0^2(\Delta\tau) \frac{1 - \cos(\omega T - \Delta\tau)}{\omega^2(T - \Delta\tau)},$$

[0313] which depends on the arrival rate λ , the mean amplitude of each pulse $E[\psi_i]$, the total area of the normalized shape function $W(\Delta\tau)$, and the time length $T - \Delta\tau$, describes the average effects of the stationary part of $x(t)$ in $[\Delta\tau, T]$ and is referred to here as the first-order statistical power density, and the second part,

$$\lambda E[\psi_i^2] \int_{-\Delta\tau, 0}^{\Delta\tau} \int_0^{\Delta\tau - |k|} y(u + |k|) y(u) du \left(1 - \frac{|k|}{T - \Delta\tau}\right) \cos(\omega k) dk,$$

[0314] which depends on the mean square amplitude of each pulse $E[\psi_i^2]$ and the shape function $y(\tau)$ in addition to λ , T , and $\Delta\tau$, describes the variational effects of the stationary part of $x(t)$ and is referred to here as the second-order statistical power density. While $E[S_1(\omega)]$ in (75) consists of two parts, the first part,

$$\frac{2\lambda^2 E^2[\psi_i]}{T + \Delta\tau} \left[\int_{-\Delta\tau, 0}^{\Delta\tau} \int_0^{\Delta\tau - |k|} y(v + |k|) y(v) dv \cos(\omega k) dk \right] \frac{1 - \cos(\omega T)}{\omega^2},$$

[0315] depends also on the shape function $y(\tau)$ as the shape function is used in calculating the power associated with the nonstationary parts of $x(t)$ in $[0, \Delta\tau]$ and $[T, T + \Delta\tau]$.

[0316] When the shape function is a delta function (i.e., $\Delta\tau \rightarrow 0$), the nonstationary parts of $x(t)$ vanish and $E[S_1(\omega)]$ in (75) can be shown to be equivalent to $E[S_2(\omega)]$ in (100). By (68) and (69), we have

$$\int_{-\Delta\tau}^{\Delta\tau} \int_0^{\Delta\tau - |k|} y(v + |k|) y(v) dv \cos(\omega k) dk = \quad (104)$$

-continued

$$\left| \int_0^{\Delta\tau} y(v) e^{-j\omega v} dv \right|^2$$

[0317] When $y(v) = W_0 \delta(v)$, where W_0 is a constant, we have from (104)

$$\lim_{\Delta\tau \rightarrow 0} \int_{-\Delta\tau}^{\Delta\tau} \int_0^{\Delta\tau - |k|} y(v + |k|) y(v) dv \cos(\omega k) dk = \quad (105)$$

$$\lim_{\Delta\tau \rightarrow 0} \left| \int_0^{\Delta\tau} W_0 \delta(v) e^{-j\omega v} dv \right|^2 = W_0^2$$

[0318] Since $|k| < \Delta\tau$ in (100), we have $|k| \rightarrow 0$ as $\Delta\tau \rightarrow 0$ and hence

$$\lim_{\Delta\tau \rightarrow 0} \left(1 - \frac{|k|}{T - \Delta\tau}\right) = 1 \quad (106)$$

[0319] Substituting (105) and (106) into (100) and noting that $W(\Delta\tau) = W_0$ when $y(v) = W_0 \delta(v)$, and substituting (105) into (75) and noting that $T + \Delta\tau \rightarrow T$ as $\Delta\tau \rightarrow 0$, yields

$$E[S_2(\omega)] = \quad (107)$$

$$E[S_1(\omega)] = 2\lambda^2 E^2[\psi_i] \frac{1 - \cos(\omega T)}{\omega^2 T} W_0^2 + \lambda E[\psi_i^2] W_0^2$$

[0320] By (104) the power spectral density in (101) can be expressed as

$$S_x(\omega) = 2\lambda^2 E^2[\psi_i] W_0^2 (\Delta\tau) \delta(\omega) + \lambda E[\psi_i^2] Y(\omega) W_0^2 \quad (108)$$

[0321] where $Y(j\omega) = \int_0^{\Delta\tau} x(t) e^{-j\omega t} dt$. When $T \rightarrow \infty$ in (75), we have by using (104)

$$\frac{S(\omega) = \lim_{T \rightarrow \infty} E[S_1(\omega)] = 2\lambda^2 E^2[\psi_i] Y(\omega) W_0^2 \delta(\omega) + \lambda E[\psi_i^2] Y(\omega) W_0^2}{[Y(\omega)]^2} \quad (109)$$

[0322] Equation (109) has a slightly different form from that of (108) because the power associated with the nonstationary parts of $x(t)$ is included in (109). When $y(t) = W_0 \delta(t)$ (108) and (109) reduce to

$$S_x(\omega) = S(\omega) = 2\lambda^2 E^2[\psi_i] W_0^2 \delta(\omega) + \lambda E[\psi_i^2] W_0^2 \quad (110)$$

[0323] Equation (110) can also be obtained from (106) by letting $T \rightarrow \infty$ and using

$$\lim_{T \rightarrow \infty} \frac{1 - \cos(\omega T)}{\omega^2 T} = \lim_{T \rightarrow \infty} \frac{2 \sin^2 \frac{\omega T}{2}}{\omega^2 T} = \lim_{T \rightarrow \infty} \frac{2 \sin^2 \frac{\omega T}{2}}{\omega^2 T} = \delta(\omega) \quad (111)$$

EXAMPLES AND NUMERICAL SIMULATION

[0324] When the shape function of the pulses is represented by a half sine wave, i.e.,

$$y(t) = \sin\left(\frac{\pi t}{\Delta\tau}\right) \left[H(t) - H(t - \Delta\tau) \right] \quad (112)$$

[0325] where $H(\cdot)$ is the Heaviside function, we obtain by using (60), (64), and (103)

$$E[X(j\omega)] = -\frac{E(\psi_1)\lambda\tau\Delta\tau(1 + e^{-\pi\Delta\tau})\pi e^{-\pi T}}{j\omega(\tau^2 - \omega^2\Delta\tau^2)} \quad (113)$$

$$E[S_1(\omega)] = \frac{2\pi^2\Delta\tau^2[1 + \cos(\omega\Delta\tau)]}{(\omega^2\Delta\tau^2 - \pi^2)^2(T + \Delta\tau)} \left[\lambda TE(\psi_1^2) - \frac{2\lambda^2 E^2(\psi_1)\cos(\omega T - 1)}{\omega^2} \right] \quad (114)$$

$$E[S_2(\omega)] = \lambda E(\psi_1^2)\Delta\tau^2 \left\{ \frac{[-2\pi^4 - 2T\cos(\omega\Delta\tau)\pi^4 + (4\cos(\omega\Delta\tau)\pi^4 + \pi^4)\Delta\tau]}{(\omega^2\Delta\tau^2 - \pi^2)^2(T + \Delta\tau)} + \frac{[+ (8\sin(\omega\tau)\omega\pi^2 + \frac{2T\cos(\omega\Delta\tau)\omega^2\pi^2 + 2T\pi^2\omega^2\Delta\tau^2}{(\omega^2\Delta\tau^2 - \pi^2)^2(T + \Delta\tau)} + \frac{[(\omega^4\Delta\tau^5 - 4\cos(\omega\Delta\tau)\omega^2\pi^2 - 2\omega^2\pi^2\Delta\tau^3)]}{(\omega^2\Delta\tau^2 - \pi^2)^2(T + \Delta\tau)} + \frac{8\lambda E^2(\psi_1)\Delta\tau^2(1 - \cos(\omega(T - \Delta\tau))}{\pi^2\omega^2(T - \Delta\tau)} \right] \quad (115)$$

[0326] Consider next the normalized shape function $y(t)$ shown in FIG. 35 with unit maximum amplitude. It is obtained by averaging a series of normalized force pulses from impact tests on the four-bay space frame as shown in FIG. 10. There are 21 sample points in the shape function, which are connected, as shown in FIG. 34. Other parameters used are $T=8$ s, $\Delta\tau=20\pi T/1024=0.15625$ s where $h=T/1024=0.0078125$ s is the sampling interval, $\lambda=4.14$ /s, $E[\psi_1]=0.8239$ N, and $E[\psi_1^2]=0.7163$ N². The curve for $E[x(t)]$ in the time interval from 0 to 8.15625 s, shown as a solid line in FIG. 36, is calculated using (81). It is seen that $E[x(t)]$ increases from 0 to 0.0352 N in the first 0.15625 s, remains at 0.0352 N from 0.15625 s to 8 s, and decreases from 0.0352 N to 0 in the last 0.15625 s. The curve for $20 \log\{E[X(j\omega)]\}$ in the frequency range from 0 to 50 Hz, shown as a dotted line in FIG. 37, is calculated using (61). The curve for $10 \log\{E[S_1(j\omega)]\}$ in the same frequency range,

shown as a solid line in FIG. 38, is calculated using (75). The curve for $10 \log\{E[S_2(j\omega)]\}$ with $\lambda=1$ /s and the other parameters unchanged is shown as a dashed line in FIG. 38. It is seen that $E[S_1(j\omega)]$ increases by 4.14 to 15.6247 times in the frequency range shown when λ is increased from $\lambda_2=1$ /s to $\lambda_1=4.14$ /s. This result can be shown by using (75)

$$\frac{\lim_{\omega \rightarrow 0} E[S_1(j\omega)]|_{\lambda=\lambda_1}}{\lim_{\omega \rightarrow 0} E[S_1(j\omega)]|_{\lambda=\lambda_2}} = \frac{\lambda_1^2 E^2[\psi_1]T^2 + \lambda_1 TE[\psi_1^2]}{\lambda_2^2 E^2[\psi_1]T^2 + \lambda_2 TE[\psi_1^2]} = \quad (116)$$

$$\frac{\lambda_1^2 E^2[\psi_1]T + \lambda_1 E[\psi_1^2]}{\lambda_2^2 E^2[\psi_1]T + \lambda_2 E[\psi_1^2]} = 15.6247$$

$$\frac{\lim_{\omega \rightarrow 0} E[S_1(j\omega)]|_{\lambda=\lambda_1}}{\lim_{\omega \rightarrow 0} E[S_1(j\omega)]|_{\lambda=\lambda_2}} = \frac{\lambda_1}{\lambda_2} = 4.14 \quad (117)$$

[0327] This shows that a larger arrival rate λ would increase the energy input to the structure over the entire frequency domain.

[0328] Numerical simulation is undertaken next to validate the analytical predictions. The random number $N(T)$ satisfying the Poisson distribution in (51) with $\lambda=4.14$ s and $T=8$ s is generated using MATLAB. Similarly, the random numbers corresponding to the random variables τ_i ($i=1, 2, \dots, N(T)$), satisfying the uniform distribution in (52), and the random numbers corresponding to the random variables ψ_i ($i=1, 2, \dots, N(T)$), satisfying the Gaussian distribution in (53) with $\mu=0.8239$ N and $\sigma^2=0.7163-0.8239^2$ N²=0.0375 N², are generated. Using the shape function constructed earlier, a sample function of $x(t)$ in (50) at time $t=rh$, where $r=0, 1, \dots$,

$$R = \lceil R = \frac{T + \Delta\tau}{h} = 1044 \rceil,$$

[0329] denoted by x_r , can be obtained. The discrete Fourier transform (DFT) of the time series $\{x_r\}$ is calculated using MATLAB. The DFT of the series $\{x_r\}$ is defined by

$$X_q = \frac{1}{R} \sum_{r=0}^{R-1} x_r e^{-j\frac{2\pi q r}{R}} \quad (118)$$

[0330] where $q=0, 1, \dots, R-1$. Equation (118) is an approximate formula for calculating the coefficients of the Fourier series of a periodic function whose values in the period $[0, T+\Delta\tau]$ are given by those of $x(t)$:

$$X_q = \frac{1}{T + \Delta\tau} \int_0^{T+\Delta\tau} x(t) e^{-j\frac{2\pi q t}{T+\Delta\tau}} dt \quad (119)$$

[0331] The Fourier components X_q correspond to harmonics of frequency

$$\omega_q = \frac{2\pi q}{T + \Delta\tau}.$$

[0332] Recall that the Fourier transform of $x(t)$ in (50) is given by

$$X(j\omega) = \int_0^{T+\Delta\tau} x(t)e^{-j\omega t} dt \quad (120)$$

[0333] Let

$$\omega = \omega_q = \frac{2\pi q}{T + \Delta\tau}$$

[0334] in (120) and compare the resulting expression with (119), we find that X_q in (118) multiplied by $T + \Delta\tau$ provides an approximate value of $X(j\omega)$ at frequency ω_q . Similarly, $X_q X_q^*$ multiplied by $T + \Delta\tau$ provides an approximate value of

$$S_1(\omega) = \frac{X(j\omega)X^*(j\omega)}{T + \Delta\tau}$$

[0335] at frequency ω_q . By averaging 5000 sample series of $\{x_n\}$, we obtain the curve for $E[x(t)]$, shown as a dotted line in FIG. 36. By averaging 1000 sample series of $\{20 \log[(T + \Delta\tau)|X_q|]\}$, we obtain the curve for $20 \log E[X(j\omega)]$, shown as a solid line in FIG. 37. By averaging 100 sample series of $\{10 \log[(T + \Delta\tau)|X_q X_q^*|]\}$, we obtain the curve for $10 \log E[S_1(j\omega)]$, shown as a dotted line in FIG. 38. The numerical results are in good agreement with the analytical ones.

[0336] The stochastic model was experimentally validated for an experimenter conducting manually a random series of impacts on the four bay space frame as shown in FIG. 10. One hundred ensemble averages were used. The experimental probability density functions of the arrival time, the number of arrived pulses, and the pulse amplitudes are in good agreement with the analytical values, as shown in FIGS. 39-41.

[0337] Thus, the system and method for detecting structural damage and the random impact series method as embodied and broadly described herein can be applied to an unlimited number and type of structures to provide automated, reliable damage detection and assessment and to conduct modal testing. This system could be further automated to conduct periodic tests and provide results to a centralized monitoring section. Regular health monitoring of these types of structures could provide additional protection against potential failure, as well as a characterization of usage and wear over time in particular environmental conditions for predicting useful service life.

[0338] The foregoing embodiments and advantages are merely exemplary and are not to be construed as limiting the

present invention. The present teaching can be readily applied to other types of systems. The description of the present invention is intended to be illustrative, and not to limit the scope of the claims. Many alternatives, modifications, and variations will be apparent to those skilled in the art. In the claims, means-plus-function clauses are intended to cover the structures described herein as performing the recited function and not only structural equivalents but also equivalent structures.

What is claimed is:

1. A system for determining stiffness parameters of a structure, comprising:

a sensor arranged to measure vibrations of said structure and output vibration information; and

a stiffness parameter unit for receiving said vibration information, determining natural frequency data of said structure, and determining the stiffness parameters of said structure using said natural frequency data.

2. The system according to claim 1, further comprising multiple sensors arranged to measure vibrations of said structure and output vibration information.

3. The system according to claim 1, wherein said stiffness parameter unit comprises an iterative processing unit.

4. The system according to claim 1, wherein said stiffness parameter unit comprises an outer iterative processing unit and an inner iterative processing unit.

5. The system according to claim 3, wherein said iterative processing unit determines said stiffness parameters using a first order perturbation process.

6. The system according to claim 3, wherein said iterative processing unit determines said stiffness parameters using a higher order perturbation process.

7. A system for determining stiffness parameters of a structure, comprising:

a sensor arranged to measure vibrations of said structure and output vibration information; and

a stiffness parameter unit for receiving said vibration information and determining said stiffness parameters with an iterative processing unit.

8. The system according to claim 7, wherein said iterative processing unit comprises an outer iterative processing unit and an inner iterative processing unit.

9. The system according to claim 7, wherein said iterative processing unit determines said stiffness parameters using a first order perturbation process.

10. The system according to claim 7, wherein said iterative processing unit determines said stiffness parameters using a higher order perturbation process.

11. A stiffness parameter unit for determining stiffness parameters for a structure, comprising:

an input for receiving vibration data related to the structure;

an analyzer for converting said vibration data to spectral data; and

an iterative processing unit for receiving said spectral data and outputting said stiffness parameters using natural frequencies of the structure.

12. A stiffness parameter unit for determining stiffness parameters for a structure, comprising:

an input for receiving vibration data related to the structure;

an analyzer for converting said vibration data to spectral data; and

an interactive processing unit for receiving said spectral data and outputting said stiffness parameters using a perturbation process.

13. The stiffness parameter unit according to claim 12, wherein said perturbation process comprises a first order perturbation process.

14. The stiffness parameter unit according to claim 12, wherein said perturbation process comprises a higher order perturbation process.

15. A system for determining damage information of a structure, comprising:

a sensor arranged to measure vibrations of said structure and output vibration information;

a stiffness parameter unit for receiving said vibration information, determining natural frequency data of said structure, and determining the stiffness parameters of said structure using said natural frequency data; and

a damage information processor for receiving said stiffness parameters and outputting damage information.

16. The system according to claim 15, wherein said damage information processor outputs damage location information or extent of damage information.

17. A system, comprising:

a structure;

a sensor arranged to measure vibrations of said structure and output vibration information; and

a stiffness parameter unit for receiving said vibration information, determining natural frequency data of said structure, and determining the stiffness parameters of said structure using said natural frequency data.

18. The system according to claim 17, further comprising a damage information processor for receiving said stiffness parameters and outputting location of damage.

19. The system according to claim 18, wherein said damage information processor comprises a damage location processor for determining damage location information.

20. The system according to claim 18, wherein said damage information processor comprises a damage extent processor for determining extent of damage information.

21. The system according to claim 18, wherein said damage information processor comprises a damage extent processor for determining extent of damage information and a damage location processor for determining damage location information.

22. The system according to claim 17, wherein said sensor comprises a velocimeter.

23. The system according to claim 17, wherein said sensor is attached to said structure.

24. The system according to claim 17, wherein said sensor is not attached to said structure.

25. The system according to claim 17, wherein said stiffness parameter unit further comprises a spectral analyzer.

26. The system according to claim 17, wherein said structure comprises a beam.

27. The system according to claim 17, wherein said structure comprises a truss.

28. The system according to claim 17, wherein said structure has a longest dimension less than 1.5 meters.

29. The system according to claim 17, wherein said structure has a longest dimension less than 2.5 meters.

30. The system according to claim 17, wherein said structure has a longest dimension less than 10 meters.

31. The system according to claim 17, wherein said structure has a longest dimension less than 50 meters.

32. A device, comprising:

a random signal generating unit for generating first and second outputs;

a random impact actuator for receiving said first and second outputs; and

an impact applicator coupled to said random impact actuator and having an impact region;

wherein said random impact actuator drives said impact applicator such that the force and arrival times of said impact applicator at said impact region are random.

33. The device of claim 32, wherein said random impact actuator drives said impact applicator in accordance with said first and second outputs.

34. The device of claim 33, wherein the first and second outputs comprise independent random variables.

35. The device of claim 34, wherein the first and second outputs determine the force and arrival times, respectively, of the impact applicator at the impact region.

36. A system, comprising:

a structure;

a random impact device for inducing vibrations in said structure;

a sensor arranged to measure vibrations of said structure and output vibration information; and

a stiffness parameter unit for receiving said vibration information, determining natural frequency data of said structure, and determining the stiffness parameters of said structure using said natural frequency data.

37. The system of claim 36, wherein the random impact device comprises:

a random signal generating unit for generating first and second outputs;

a random impact actuator for receiving said first and second outputs; and

an impact applicator coupled to said random impact actuator and having an impact region;

wherein said random impact actuator drives said impact applicator such that the force and arrival times of said impact applicator at said impact region are random.

38. The device of claim 37, wherein said random impact actuator drives said impact applicator in accordance with said first and second outputs.

39. The device of claim 38, wherein the first and second outputs comprise independent random variables.

40. The device of claim 39, wherein the first and second outputs determine the force and arrival times, respectively, of the impact applicator at the impact region.

41. A system for determining stiffness parameters of a structure, comprising:

a sensor arranged to measure vibrations of said structure and output vibration information; and

a stiffness parameter unit for receiving said vibration information, determining mode shape information, and determining the stiffness parameters of said structure using said mode shape information.

42. The system according to claim 41, further comprising multiple sensors arranged to measure vibrations of said structure and output vibration information.

43. The system according to claim 41, wherein said stiffness parameter unit comprises an iterative processing unit.

44. The system according to claim 41, wherein said stiffness parameter unit comprises an outer iterative processing unit and an inner iterative processing unit.

45. The system according to claim 43, wherein said iterative processing unit determines said stiffness parameters using a first order perturbation process.

46. The system according to claim 43, wherein said iterative processing unit determines said stiffness parameters using a higher order perturbation process.

* * * * *